

# The Quasar Feedback Survey: Revealing the importance of sensitive radio imaging for AGN identification deeper into the radio-quiet regime

Ann Njeri,<sup>1</sup>★ Chris M. Harrison,<sup>1</sup>† Preeti Kharb,<sup>2</sup> David M. Alexander,<sup>3</sup> Vincenzo Mainieri,<sup>4</sup> Chiara Circosta,<sup>5</sup>

Victoria A. Fawcett,<sup>1</sup> Darshan Kakkad,<sup>6</sup> Dipanjan Mukherjee,<sup>7</sup> Stephen Molyneux<sup>8,9</sup> and Silpa Sasikumar<sup>10</sup>

<sup>1</sup>*School of Mathematics, Statistics and Physics, Newcastle University, Newcastle upon Tyne, NE1 7RU, UK*

<sup>2</sup>*National Centre for Radio Astrophysics (NCRA) - Tata Institute of Fundamental Research (TIFR), S. P. Pune University Campus, Post Bag 3, Ganeshkhind, 411007 Pune, India*

<sup>3</sup>*Centre for Extragalactic Astronomy, Department of Physics, Durham University, South Road, Durham, DH1 3LE, UK*

<sup>4</sup>*European Southern Observatory (ESO), Karl-Schwarzschild-Straße 2, 85748 Garching bei München, Germany*

<sup>5</sup>*Institut de Radioastronomie Millimétrique (IRAM), 300 rue de la Piscine, 38400 Saint-Martin-d'Hères, France*

<sup>6</sup>*Centre for Astrophysics Research, Department of Physics, Astronomy and Mathematics, University of Hertfordshire, Hatfield, AL10 9AB, UK*

<sup>7</sup>*Inter-University Centre for Astronomy and Astrophysics, Post Bag - 4, Pune University, Ganeshkhind, Pune - 411007, India*

<sup>8</sup>*School of Physics and Astronomy, University of Southampton, Southampton, SO17 1BJ, UK*

<sup>9</sup>*Institute of Theoretical Astrophysics, University of Oslo, P.O. Box 1029, Blindern, 0315 Oslo, Norway*

<sup>10</sup>*Departamento de Astronomía, Universidad de Concepción, Concepción, Chile*

Accepted 2026 January 9. Received 2025 January 7; in original form 2025 October 6

## ABSTRACT

We present new sub-arcsecond ( $\sim 0.3\text{--}1$  arcsec;  $\sim 1\text{--}3$  kpc) VLA imaging at 1.4 GHz and 6 GHz of 29 optically-selected, [O III] luminous ( $L_{\text{[OIII]}} > 10^{42.1}$  erg s $^{-1}$ ),  $z < 0.2$  quasars drawn from the expanded Quasar Feedback Survey (QFeedS; with  $L_{1.4\text{GHz}} = 10^{22.6}\text{--}10^{26.3}$  W Hz $^{-1}$ ). These 29 new objects occupy the low end of the radio-power distribution ( $L_{1.4\text{GHz}}=10^{22.63}\text{--}10^{23.45}$  W Hz $^{-1}$ ) in the QFeedS sample and are nominally ‘radio quiet’. Despite this, we find widespread evidence of AGN-driven synchrotron activity. Nearly  $\sim 31$  per cent exhibit resolved radio structures on  $\sim 0.1\text{--}20$  kpc scales consistent with compact jets or wind-driven outflows, and  $\sim 90$  per cent display steep spectra ( $\alpha \lesssim -1$ ) indicative of optically thin synchrotron emission. Combining morphology, spectral index and brightness-temperature diagnostics, at least  $\sim 38$  per cent of the sample show clear AGN signatures that cannot be explained by star formation alone. These constitute the first results from the expanded QFeedS (now 71 quasars spanning  $\sim 4$  dex in radio power) and demonstrate that compact, low-power jets and AGN shocks are common deep inside the radio-quiet regime. A thorough understanding of feedback processes from quasars, deep into the ‘radio-quiet’ regime, will be obtained by connecting these high resolution radio observations with multi-wavelength observations.

**Key words:** galaxies: evolution – galaxies: active – galaxies: jets – quasars: supermassive black holes – radio continuum: galaxies

## 1 INTRODUCTION

The radio-quiet quasar population is the predominant sample in optically-selected quasar samples, such as those from the Sloan Digital Sky Survey (SDSS; Kellermann et al. 2016). Despite being among the most luminous optical sources, radio-quiet quasars remain challenging to study in the radio due to their intrinsically weak emission, compact morphology, and ambiguous emission mechanisms (e.g. Padovani 2016; Panessa et al. 2019). These luminous active galactic nuclei (AGN) remain largely unresolved at the spatial resolution

of all sky radio surveys such as FIRST and NVSS<sup>1</sup> (e.g. Tadhunter 2016; Kellermann et al. 2016; McCaffrey et al. 2022), meaning that the radio emission is typically confined within the host galaxies, i.e., on scales smaller than a few kiloparsecs. However, extended radio structures with an AGN origin may exist on smaller scales if produced by jets or shocks due to AGN-driven outflows, that are young and/or frustrated by a dense interstellar medium (e.g. Panessa et al. 2019; Klindt et al. 2019; Fawcett et al. 2020).

Despite the lack of powerful radio jets, it is becoming increasingly clear that studying radio emission in detail is very important for understanding the feedback processes from radio-quiet quasars. For ex-

★ E-mail: ann.njeri@newcastle.ac.uk

† E-mail: christopher.harrison@newcastle.ac.uk

<sup>1</sup> These are the Faint Images of the Radio Sky at Twenty-cm survey (FIRST) and the NRAO VLA Sky Survey (NVSS) (Becker et al. 1995; Condon et al. 1998)

ample, hydrodynamic simulations have demonstrated that low-power radio jets, characteristic of radio-quiet AGN, can still exert significant influence on their host galaxies. This is particularly through their interactions with the interstellar medium (ISM) when the jets are closely inclined relative to the galactic disk and can drive strong shocks and accelerate the gas (e.g., Meenakshi et al. 2022; Tanner & Weaver 2022; Mukherjee 2025). Importantly, jets do not need to escape the host galaxy to affect star formation. Even when confined within the inner kiloparsecs, these jets can cause turbulence, heat cold gas, and regulate the local gas reservoir. These theoretical insights are particularly relevant for compact low-luminosity radio sources, whose sub-kpc sizes and steep spectral indices are consistent with jet-ISM interactions occurring at  $< 2$  kpc scales, potentially in early or frustrated phases of feedback (e.g. Chilufya et al. 2024; Njeri et al. 2025). Furthermore, quasar-driven winds could cause similar signatures in the extended radio emission, since they propagate as multi-phase outflows through the ISM, shocking the material to produce synchrotron emission (e.g., Zakamska et al. 2016; Nims et al. 2015; Meenakshi et al. 2024). While these processes can mimic starburst-driven outflows in the optical line kinematics, careful radio morphological and spectral analysis, such as identifying steep-spectrum, compact structures, and high brightness temperatures, can distinguish AGN from star formation origins (e.g. Jarvis et al. 2021; Morabito et al. 2022; Njeri et al. 2025).

A key open question in galaxy evolution is the contribution to feedback from low-power and compact radio jets and quasar-driven winds in radio-quiet quasars. While classical radio-loud quasars with powerful jets are well established as efficient regulators of gas cooling for massive galaxies (e.g. Heckman & Best 2014; Fabian 2012; Harrison 2017), the impact of faint or compact structures such as frustrated jets and disk winds, remains less clear (e.g. Laor & Behar 2008; Panessa et al. 2019; Baldi 2023). Recent studies suggest that even in radio-quiet quasars, small-scale jets and outflows can efficiently couple to the ISM on small scales, driving turbulence and modest outflows (e.g. Venturi et al. 2021; Jarvis et al. 2019; Kharb & Silpa 2023; Cresci et al. 2023; Morganti et al. 2023; Audibert et al. 2023; Ulivi et al. 2024; Mukherjee 2025). Determining whether such processes represent a significant feedback mode, and how efficiently they regulate star formation, is crucial for building a complete picture of AGN-galaxy co-evolution.

A related challenge, is how can we robustly separate star formation from AGN-driven radio emission, and establishing what this reveals about the spectrum of feedback modes in quasars. This complicates efforts to assess the star-formation rates at quasar luminosities and raises questions about how feedback scales across the radio luminosity function. The emerging view is that quasars span a continuum of radio modes, from weak, AGN-contaminated synchrotron at low luminosities to powerful jet-dominated systems at high luminosities (e.g. Zakamska & Greene 2014; Sabater et al. 2019; Jarvis et al. 2021; Girdhar et al. 2022; Slob et al. 2022). This spectrum challenges the traditional binary classification of ‘radio-loud’ versus ‘radio-quiet’ AGN and motivates a more continuum between accretion states, production of radio emission, and efficiency of feedback (e.g. Padovani 2017; Hardcastle & Croston 2020; Mingo et al. 2022).

Towards addressing the outstanding issues outlined above, we have been undertaking a systematic survey of low redshift Type 1 and Type 2 ( $z < 0.2$ ) quasars, called the “Quasar Feedback Survey” (QFeedS; Jarvis et al. 2021)<sup>2</sup>. The primary objectives of this survey include: (1) understanding the origin of radio emission in sources with moderate-

to-low radio luminosities; (2) characterizing the properties of multi-phase outflows in the quasar host galaxies; and, (3) assessing the potential long-term impact of the central quasar on the host galaxies.

In this work we introduce our first results on the radio properties from a new sample, exploring deeper into the radio-quiet regime ( $L_{1.4\text{GHz}} < 10^{23.4} \text{ W Hz}^{-1}$ ) than our earlier work ( $L_{1.4\text{GHz}} > 10^{23.4} \text{ W Hz}^{-1}$ ). In Section 2 we introduce the Quasar Feedback Survey (QFeedS) and describe the new sample for this current work (QFeedS-2). In Section 3 we describe the observations and imaging methods for the new radio data, before discussing the results in Section 4. In Section 5 we discuss our new results in the context of the wider QFeedS sample and other AGN populations and present our main conclusions in Section 6. We adopt  $H_0 = 70 \text{ km s}^{-1} \text{ Mpc}^{-1}$ ,  $\Omega_M = 0.3$ ,  $\Omega_\Lambda = 0.7$  throughout. In this cosmology, 300 mas (i.e., our typical resolution at  $\sim 6.0 \text{ GHz}$ ), corresponds to  $\sim 0.8 \text{ kpc}$  for the median redshift of the sample ( $z=0.15$ ). We define the radio spectral index,  $\nu$ , using  $S_\nu \propto \nu^\alpha$ .

## 2 THE QUASAR FEEDBACK SURVEY

In this section we present an overview of QFeedS and the motivation for the new sample (Section 2.1), before describing in more detail the sample used in this work (Section 2.2 and Section 2.3).

### 2.1 Survey description

The initial sample of 42 quasars (QFeedS-1) was fully introduced in Jarvis et al. (2021), although this followed multiple pilot studies (e.g., Harrison et al. 2014, 2015; Lansbury et al. 2018; Jarvis et al. 2019). The goal of QFeedS is to build up a multi-wavelength picture of feedback from quasars; e.g., covering radio imaging, and multi-phase outflow measurements. Quasars for QFeedS are selected to be low redshift ( $z < 0.2$ ) luminous [O III] emitters ( $L_{[\text{OIII}]} \gtrsim 10^{42} \text{ erg s}^{-1}$ ) from the AGN sample presented in Mullaney et al. (2013), who used spectroscopy from the SDSS, Data Release 7 (Abazajian et al. 2009). This redshift and luminosity selection criteria enables high spatial resolution observations (reaching sub-kiloparsec resolution) of sources that have quasar-like AGN luminosities ( $L_{\text{AGN}} \gtrsim 10^{45} \text{ erg s}^{-1}$ ). These luminosities are equivalent to the knee of the luminosity function around cosmic noon (see Jarvis et al. 2020, 2021). Therefore, this survey is complementary to surveys of more nearby radiatively luminous AGN, which cover typically lower bolometric powers or smaller samples (e.g., Riffel et al. 2017; Rose et al. 2018; Davies et al. 2020; Venturi et al. 2021; García-Burillo et al. 2021; Fluetsch et al. 2021), or those that focus on radio galaxies (e.g., Morganti et al. 2005; Santoro et al. 2020; Speranza et al. 2021). It also complements those that focus on higher redshifts, which reach higher luminosities but with more limited sensitivity and spatial resolution (e.g., Nesvadba et al. 2017; Circosta et al. 2018; Roy et al. 2025; Ilha et al. 2025).

Similar surveys at the redshift range of QFeedS, also cover multi-wavelength approaches to understanding AGN feedback in quasars (e.g., Karouzos et al. 2016; Ramos Almeida et al. 2022; Bessiere et al. 2024). However, unlike most other surveys of radiatively luminous AGN, a key part of QFeedS has been to start by obtaining complete coverage with high spatial resolution radio imaging. Specifically, we have focused on the C-band (4–8 GHz) and L-band (1–2 GHz) from

<sup>2</sup> A survey website, including results, information on targets and open access

to our data products/images can be found here: (<https://blogs.ncl.ac.uk/quasarfeedbacksurvey/>)

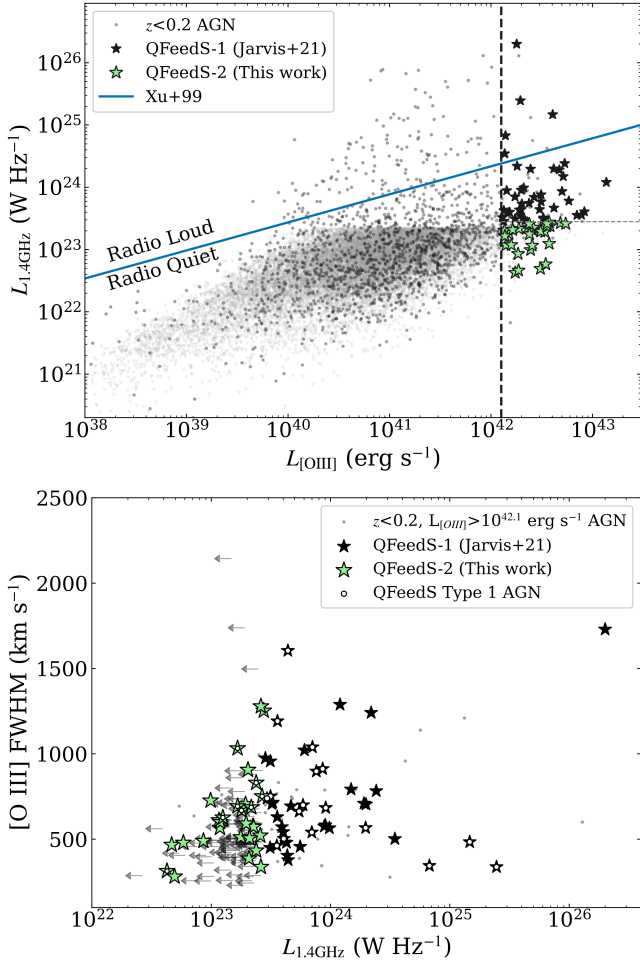


**Figure 1.** Top: 1.4 GHz radio luminosity versus [O III] luminosity for the parent sample of  $z < 0.2$  AGN (grey circles, with radio upper limits represented as lighter grey triangles; Mullaney et al. 2013). The dashed vertical line shows our quasar luminosity threshold for selection ( $L_{[\text{OIII}]} > 10^{42.11} \text{ erg s}^{-1}$ ). Bottom: [O III] FWHM versus 1.4 GHz radio luminosity for the parent sample above the [O III] luminosity cut (grey dots, with upper limits represented as arrows). In both panels the initial 42 QFeedS targets are represented with black stars (QFeedS-1), for which we imposed a minimum radio luminosity threshold ( $L_{1.4\text{GHz}} > 10^{23.45} \text{ W Hz}^{-1}$ ; dashed horizontal line in top panel). The 29 new targets, which are selected to be below this radio luminosity (QFeedS-2), are represented with green stars. Type 1 quasars are highlighted with white circles in the bottom panel.

both the Very Large Array (VLA; Jarvis et al. 2019, 2021) and *e*-MERLIN (Njeri et al. 2025). Combining these new observations, with data from NVSS and FIRST, this has enabled us to create multi-frequency radio images of these quasars, which are sensitive to structures on scales of  $\sim 0.05$  arcseconds (i.e.,  $\sim 0.1$  kpc) to several arcseconds (i.e., 10s kpc).

Our initial sample of 42 targets (QFeedS-1) was selected to have radio luminosities of  $L_{1.4\text{GHz}} > 10^{23.45} \text{ W Hz}^{-1}$ . The sample is presented in an [O III] luminosity versus 1.4 GHz luminosity plane in Fig. 1. It can be seen that, despite a minimum radio luminosity cut, the majority ( $\sim 90$  per cent) are still consistent with traditional definitions of ‘radio quiet’ (see discussion in Jarvis et al. 2021). However, based on a variety of radio-AGN selection criteria (i.e., radio morphology, radio-infrared excess parameter, core spectral indices and

brightness temperatures),  $86^{+4.6}_{-6.2}$  per cent reveal a radio-AGN (Jarvis et al. 2021; Njeri et al. 2025). Furthermore, radio sizes are 0.03–65 kpc, covering the same size range of archetypal compact radio galaxy populations (e.g. An & Baan 2012), but with 1–3 orders-of-magnitude lower radio luminosities. Two-thirds of the sample show distinct radio structures, often indicative of jets and lobes (e.g., see Fig. 4 in Jarvis et al. 2021 and Fig. 7 in Njeri et al. 2025). These results highlight the important contribution of AGN to the radio emission of quasars even with moderate radio luminosities (i.e., for ‘radio-quiet’ quasars; also see e.g., White et al. 2015; Zakamska et al. 2016; White et al. 2017).

Follow-up multi-wavelength observations of QFeedS-1 targets give insight into feedback mechanisms in these sources. For example, spatially unresolved sub-mm emission-line observations suggest little immediate impact on the global molecular gas reservoirs in the host galaxies by the quasars in these systems (Jarvis et al. 2020; Molyneux et al. 2024). However, spatially-resolved observations show a strong localized connection between the radio structures and high levels of turbulence and outflows, revealed through optical integral field spectroscopy (Harrison et al. 2015; Jarvis et al. 2019; Girdhar et al. 2022); sub-mm interferometry (Girdhar et al. 2022, 2024); and X-rays (Lansbury et al. 2018). Follow-up polarisation-sensitive radio imaging has revealed a high fractional polarization (10–30 per cent) in the sources with the largest radio lobes, which provides further evidence of an interplay of jets or winds and emission-line gas as an important contribution to the nature of radio outflows in radio-quiet AGN (Silpa et al. 2022). These observations are broadly consistent with simulations that show low power jets, confined within galaxy disks can drive outflows and have a feedback effect on their hosts, with potential additional contributions from outflow-driven shocks (e.g. Mukherjee et al. 2018; Tanner & Weaver 2022; Meenakshi et al. 2022, 2024).

The results from QFeedS-1 reveal important information on the prevalence of radio AGN and how feedback works in a sample of mostly traditionally radio-quiet quasars. However, we are unable to address how representative these results are to the wider quasar population, reaching lower radio luminosities. Therefore in this work, we present a new sample, QFeedS-2, reaching an order of magnitude lower in radio power and place them even more completely into the context of other AGN populations (following e.g., Jarvis et al. 2021; Hardcastle & Croston 2020; Baldi 2023).

## 2.2 Sample selection for this work

Our goal is to expand the survey selection for QFeedS presented in Jarvis et al. (2021), to quasars with lower radio luminosities.<sup>3</sup> Therefore, we follow Jarvis et al. (2021), and choose  $z < 0.2$  AGN from Mullaney et al. (2013) with a luminosity  $L_{[\text{OIII}]} > 10^{42.11} \text{ erg s}^{-1}$ . This leaves a potential sample of 226 targets. We then exclude any sources with a declination between 24 and 44 degrees, to avoid observing targets that transit with very high elevations above the VLA.<sup>4</sup>

<sup>3</sup> We calculate the radio luminosities using the 1.4 GHz flux densities for each source provided by Mullaney et al. (2013) (i.e., those taken from NVSS with preference, or FIRST otherwise) and assuming a spectral index of  $\alpha = -0.7$ . For the non radio detected sources, we use a flux density of 2.5 mJy to derive luminosity upper limits, corresponding to the 50% completeness of the NVSS survey (Condon et al. 1998)

<sup>4</sup> We note that for the initial sample we also only considered targets in the RA range of 10–360 degrees, for more efficient observation scheduling.

For the initial sample of 42 targets we applied a radio luminosity selection of  $L_{1.4\text{GHz}} > 10^{23.45} \text{ W Hz}^{-1}$ . These 42 sources, are labeled as “QFeedS-1” in a  $L_{1.4\text{GHz}}$  versus  $L_{[\text{OIII}]}$  diagram in the top panel of Fig. 1. To create the new sample, we observed the remaining 29 sources that have a 1.4 GHz detection (in NVSS or FIRST) but with luminosities below the  $L_{1.4\text{GHz}} = 10^{23.45} \text{ W Hz}^{-1}$  luminosity threshold. The lower luminosity sample, which is new for this work, is labeled as “QFeedS-2” in Figure 1. We list key properties of the new QFeedS-2 sample in Table 1.

### 2.3 New sample overview

This new work brings our total sample in the QFeedS to  $71 z < 0.2$  targets, all of which have been selected to have high  $[\text{O III}]$  luminosities, corresponding to bolometric luminosities of  $L_{\text{bol}} \gtrsim 10^{45} \text{ erg s}^{-1}$  (see Jarvis et al. 2020). Of the 29 targets in QFeedS-2, eight are classified as Type 1 and 21 are classified as Type 2 based on their optical spectroscopy (Mullaney et al. 2013). Across the combined sample (QFeedS-1 and QFeedS-2), 25 (35 per cent) are classified as Type 1 and 46 (65 per cent) are classified as Type 2. This is representative of the parent sample of AGN from Mullaney et al. 2013, which meet the redshift and  $[\text{O III}]$  luminosity cuts, for which 88/226 (i.e., 39 per cent) are confirmed as Type 1 AGN.

For our  $[\text{O III}]$  luminosity and redshift selection criteria (see Fig. 1);  $52_{-3.3}^{+3.3}$  per cent of the parent sample have radio detections in FIRST/NVSS from Mullaney et al. (2013). Our combined sample still does not represent the targets from the parent sample that only have upper limits on their 1.4 GHz radio luminosities based on FIRST and NVSS. The non radio detected sources have a mean upper limit of  $1.9 \times 10^{23} \text{ W Hz}^{-1}$ , with a range of  $(0.27\text{--}2.7) \times 10^{23} \text{ W Hz}^{-1}$ . Nonetheless, the combined QFeedS sample covers nearly four orders of magnitude in radio luminosity from  $L_{1.4\text{GHz}}=10^{22.6}$  to  $10^{26.3} \text{ W Hz}^{-1}$ . Indeed, the sample expands deep into the ‘radio-quiet’ regime following the definition of Xu et al. (1999) (see blue line in Fig. 1).

All targets in the QFeedS-2 sample are classified as ‘radio quiet’, with at least one order of magnitude lower radio luminosities than the ‘radio-loud’ cut off. For the Type 1 targets, we additionally investigated the radio-loudness parameter,  $R$ , which compares radio to optical continuum luminosity as a means to define sources as ‘radio loud’. Following Kellermann et al. (1989); Ivezić et al. (2002),  $R = 0.4(m_i - t)$ , where  $m_i$  is the  $i$ -band magnitude from SDSS DR16 (Ahumada et al. 2020) and  $t$  is the ‘AB radio magnitude’ given by  $t = -2.5 \log \left( \frac{S_{1.4\text{GHz}}}{3631\text{Jy}} \right)$ , none of the Type 1 targets in QFeedS-2 pass the radio-loudness criteria of  $R \gtrsim 1.0$ . In contrast, in the initial sample (QFeedS-1), 9 targets were classified as ‘radio loud’ following both criteria. Furthermore, many targets in the QFeedS-1 sample could be classified as ‘radio intermediate’, due to their proximity to the radio-loud/quiet boundary (Jarvis et al. 2021).

In the bottom panel of Figure 1 we show  $[\text{O III}]$  FWHM as a function of radio luminosity for the parent sample in the redshift and  $[\text{O III}]$  luminosity range of our selection, and highlight the QFeedS targets with larger symbols. In this figure the plotted FWHM is the flux-weighted average of the two components that are fitted to the  $[\text{O III}]$  emission lines in the SDSS spectra, following Mullaney et al. (2013). It can be seen that the combined QFeedS sample covers the full range of FWHM parameter space of the parent sample. Furthermore, the figure re-highlights the previously identified increased fraction of extreme kinematics ( $\gtrsim 800 \text{ km s}^{-1}$ ) for radio luminosities greater than  $\sim 2 \times 10^{23} \text{ W Hz}^{-1}$  (Mullaney et al. 2013; also see Zakamska & Greene 2014, Woo et al. 2016, Jarvis et al. 2021).

The new QFeedS-2 sample provides the opportunity to study the radio properties of quasars over multiple orders of magnitude in radio luminosity, and explore deep into the ‘radio-quiet’ regime. Building on the work with QFeedS-1, future multi-wavelength follow-up observations will enable an assessment of the connection between radio emission and multi-phase outflows across the quasar population. In this work, we present new L-band and C-band VLA observations of the 29 QFeedS-2 targets, following similar approaches to the equivalent data presented for the initial 42 QFeedS-1 targets in (Jarvis et al. 2019, 2021) and with C-band *e*-MERLIN data in Njeri et al. (2025). We then combine and compare the radio properties of the full sample (QFeedS-1 and QFeedS-2), and explore the possible origin of the radio emission across the full radio luminosity range.

## 3 OBSERVATIONS AND DATA REDUCTION

Observations of the 29 quasars (QFeedS-2) were conducted with VLA in the L-band (1.2 – 1.7 GHz) and C-band (5.25 – 7.20 GHz), under the proposal ID 23A-214 [PI. Njeri]. These observations were carried out between July and September 2023 using the A array, providing a representative resolution of 1.0 and 0.3 arcsec, in the L-band and C-band, respectively. Whilst all targets were covered by the C-band observations, three targets were not observed in the L-band (J0213+0042, J0232–0811, and J2304–0841), due to incomplete observations. We observed for 10.5 hours in L-band (5–30 min per source) and 9.5 hours in C-band (5–30 min per source). Each target was observed in at least two scans spread across 1 – 2 hour observing blocks. At the start of each observing block, a standard calibrator (3C286, 3C48 or 3C147) was observed for  $\sim 10$  minutes. A phase calibrator was observed for  $\sim 3$  minutes per scan (including the slewing time) followed by the target.

We used the VLA Calibration Pipeline 2024.1.0.8 for *casa* version 6.6.1 to reduce our data. The calibrated measurement set was then inspected using *casa* task PLOTMS and any remaining bad data was visually identified and flagged using ‘tfcrop’ mode in *casa* task FLAGDATA. Each target was split into their own measurement set and imaged using *casa* task TCLEAN. Maps of  $2500 \times 2500$  cells were constructed, with a cell size of 0.2 arcsecs per pixel for L-band, and 0.06 arcsecs per pixel for C-band. To produce a consistent set of images to QFeedS-1 we followed Jarvis et al. (2021) and used a Briggs weighting of  $r = 0.5$  for all radio maps. This provides a suitable compromise between sensitivity to larger scale structures and higher spatial resolution. This uniform approach is most suitable for this systematic study, but we note that a source-by-source imaging optimisation can sometimes reveal additional structures or detail (e.g., comparing different approaches for the same targets in Jarvis et al. 2021 and Jarvis et al. 2019). We generated radio maps with typical median root-mean square (rms) sensitivities of  $\sim 24 \text{ }\mu\text{Jy beam}^{-1}$  in L-band and  $\sim 10 \text{ }\mu\text{Jy beam}^{-1}$  in C-band. In comparison, the QFeedS-1 radio maps were produced at typical median rms sensitivities of  $\sim 47 \text{ }\mu\text{Jy}$  in L-band and  $\sim 12 \text{ }\mu\text{Jy beam}^{-1}$  in C-band.

Examples of these radio maps are presented in Figure 2 and Figure 3, which showcase a range of the morphological structures observed (see Section 4.1). The background optical images are from the archival 3-colour (RGB) image from the Dark Energy Spectroscopic Instrument (DESI) Legacy Imaging Survey using the  $z, r, g$  bands (Dey et al. 2019). Overlaid, are contour maps from the VLA FIRST survey in white, and our VLA L-band and C-band maps in green and blue, respectively. We release all the equivalent figures for the whole sample and all the radio maps, which include all of the

**Table 1.** Key properties for the 29 QFeedS-2 targets. (1) Source ID; (2-3) optical positions (J2000); (4) redshifts from SDSS DR7; (5) AGN Type from the optical spectra; (6-7) [O III] luminosity and FWHM from [Mullaney et al. \(2013\)](#); (8-9) integrated 1.4 GHz flux density and peak flux density from FIRST; (10) 1.4 GHz radio luminosity (based on NVSS; [Mullaney et al. 2013](#))

Source ID	RA	DEC	$z$	Type	$\log(L_{\text{[OIII]}})$ (/erg s $^{-1}$ )	FWHM <sub>[OIII]</sub> (km s $^{-1}$ )	$S_{\text{FIRST}}$ (mJy)	$P_{\text{FIRST}}$ (mJy beam $^{-1}$ )	$\log(L_{1.4 \text{ GHz}})$ (/W Hz $^{-1}$ )
(1)	(2)	(3)	(4)	(5)	(6)	(7)	(8)	(9)	(10)
J0213+0042	02:13:59.78	+00:42:26.8	0.182	1	42.68	752	2.90 $\pm$ 0.12	3.16 $\pm$ 0.07	23.43
J0232-0811	02:32:24.25	-08:11:40.2	0.100	2	42.15	567	3.48 $\pm$ 0.12	3.77 $\pm$ 0.08	23.07
J0827+2233	08:27:11.22	+22:33:24.2	0.173	2	42.37	576	2.03 $\pm$ 0.13	2.03 $\pm$ 0.07	23.35
J0841+0101	08:41:35.09	+01:01:56.3	0.111	2	42.41	388	3.51 $\pm$ 0.19	2.50 $\pm$ 0.09	23.32
J0924+1504	09:24:35.36	+15:04:10.0	0.125	2	42.39	727	3.43 $\pm$ 0.09	3.22 $\pm$ 0.05	22.99
J0947+1005	09:47:33.22	+10:05:08.8	0.139	1	42.18	669	1.41 $\pm$ 0.10	1.21 $\pm$ 0.05	23.25
J1034+6001	10:34:08.60	+60:01:52.2	0.051	2	42.41	612	18.98 $\pm$ 0.19	16.78 $\pm$ 0.10	23.06
J1110+5848	11:10:15.25	+58:48:46.0	0.143	2	42.42	574	4.11 $\pm$ 0.21	3.90 $\pm$ 0.12	23.35
J1141+2156	11:41:16.16	+21:56:21.8	0.063	1	42.24	314	2.68 $\pm$ 0.45	1.80 $\pm$ 0.20	22.63
J1152+1016	11:52:45.66	+10:16:23.8	0.070	2	42.27	468	3.57 $\pm$ 0.08	3.39 $\pm$ 0.05	22.67
J1203+1624	12:03:00.20	+16:24:43.8	0.166	2	42.74	339	2.91 $\pm$ 0.13	2.90 $\pm$ 0.07	23.42
J1300+5454	13:00:38.10	+54:54:36.9	0.088	2	42.49	282	2.16 $\pm$ 0.13	1.96 $\pm$ 0.07	22.69
J1316+4452	13:16:39.75	+44:52:35.1	0.091	2	42.20	602	4.30 $\pm$ 0.13	3.96 $\pm$ 0.07	23.07
J1325+1137	13:25:52.16	+11:37:09.8	0.161	1	42.58	831	2.84 $\pm$ 0.10	2.93 $\pm$ 0.06	23.38
J1338+1503	13:38:06.53	+15:03:56.1	0.185	2	42.53	705	2.22 $\pm$ 0.09	1.91 $\pm$ 0.05	23.29
J1355+5612	13:55:16.55	+56:12:44.7	0.122	1	42.28	688	6.04 $\pm$ 0.15	5.88 $\pm$ 0.08	23.34
J1410+2233	14:10:41.50	+22:33:37.1	0.173	1	42.14	1033	3.11 $\pm$ 0.19	2.23 $\pm$ 0.09	23.22
J1419+1144	14:19:43.79	+11:44:26.2	0.124	2	42.27	491	2.94 $\pm$ 0.13	2.54 $\pm$ 0.07	22.93
J1426+1040	14:26:14.62	+10:40:13.0	0.137	2	42.38	513	1.96 $\pm$ 0.12	2.03 $\pm$ 0.07	23.25
J1426+1949	14:26:26.93	+19:49:54.4	0.175	2	42.13	906	1.15 $\pm$ 0.06	1.44 $\pm$ 0.04	23.31
J1434+5016	14:34:11.18	+50:16:40.8	0.199	2	42.38	522	2.75 $\pm$ 0.13	2.84 $\pm$ 0.08	23.41
J1440+5303	14:40:38.10	+53:30:15.9	0.038	2	42.49	593	59.21 $\pm$ 0.30	57.20 $\pm$ 0.17	23.29
J1450+0713	14:50:34.12	+07:31:32.3	0.154	2	42.22	507	1.71 $\pm$ 0.27	1.56 $\pm$ 0.15	23.32
J1507+0029	15:07:19.94	+00:29:05.0	0.182	2	42.57	1254	4.36 $\pm$ 0.11	4.40 $\pm$ 0.06	23.44
J1529+5616	15:29:07.46	+56:16:06.7	0.100	1	42.57	627	4.26 $\pm$ 0.13	4.31 $\pm$ 0.08	23.10
J1543+1148	15:43:03.83	+11:48:38.5	0.098	2	42.54	479	2.09 $\pm$ 0.11	2.60 $\pm$ 0.07	22.77
J1653+2349	16:53:15.05	+23:49:43.0	0.103	2	42.55	435	7.14 $\pm$ 0.12	6.72 $\pm$ 0.07	23.38
J1713+5729	17:13:50.32	+57:29:54.9	0.113	2	42.55	1278	7.38 $\pm$ 0.09	7.29 $\pm$ 0.05	23.42
J2304-0841	23:04:43.48	-08:41:08.6	0.047	1	42.14	693	21.51 $\pm$ 0.75	17.85 $\pm$ 0.38	23.22

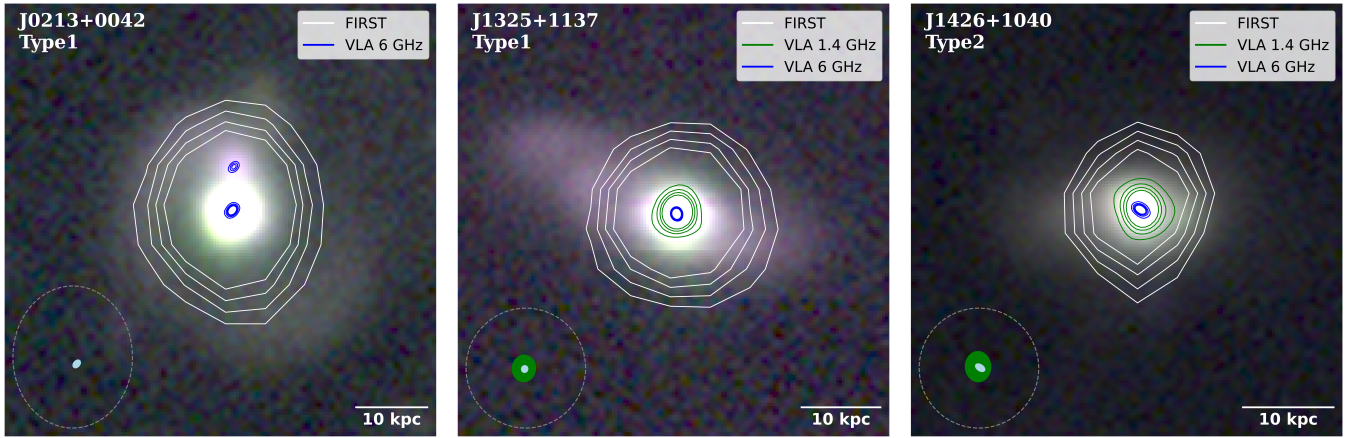


**Figure 2.** Examples of our radio data for sources classified as compact based on radio morphology in the QFeedS-2 sample (see Section 4.1). The rgb images come from the DESI Legacy Imaging Survey in the  $z$ ,  $r$ ,  $g$  bands. The contours overlaid represent: FIRST maps in white with levels  $1\sigma \times [2, 3, 4, 5]$ ; our new VLA 1.4 GHz maps in green with levels  $1\sigma \times [2, 4, 6, 8]$  (except for J0213+0042, which was not observed); and our new VLA 6 GHz maps in blue with levels  $1\sigma \times [2, 4, 6, 8]$ . Ellipses represent the synthesised beam for the corresponding radio map contours;  $\sim 5$  arcsec for FIRST (in dashed grey ellipses),  $\sim 1$  arcsec for VLA 1.4 GHz (in green) and  $\sim 0.3$  arcsec for VLA 6 GHz (in light blue). The scale bar highlights the physical size scales. Equivalent figures for all sources are provided (see the Data Availability section). For J0213+0042, we note the target was classified as a ‘compact’ source because the second radio component, which coincides with a second optical companion, was ignored.

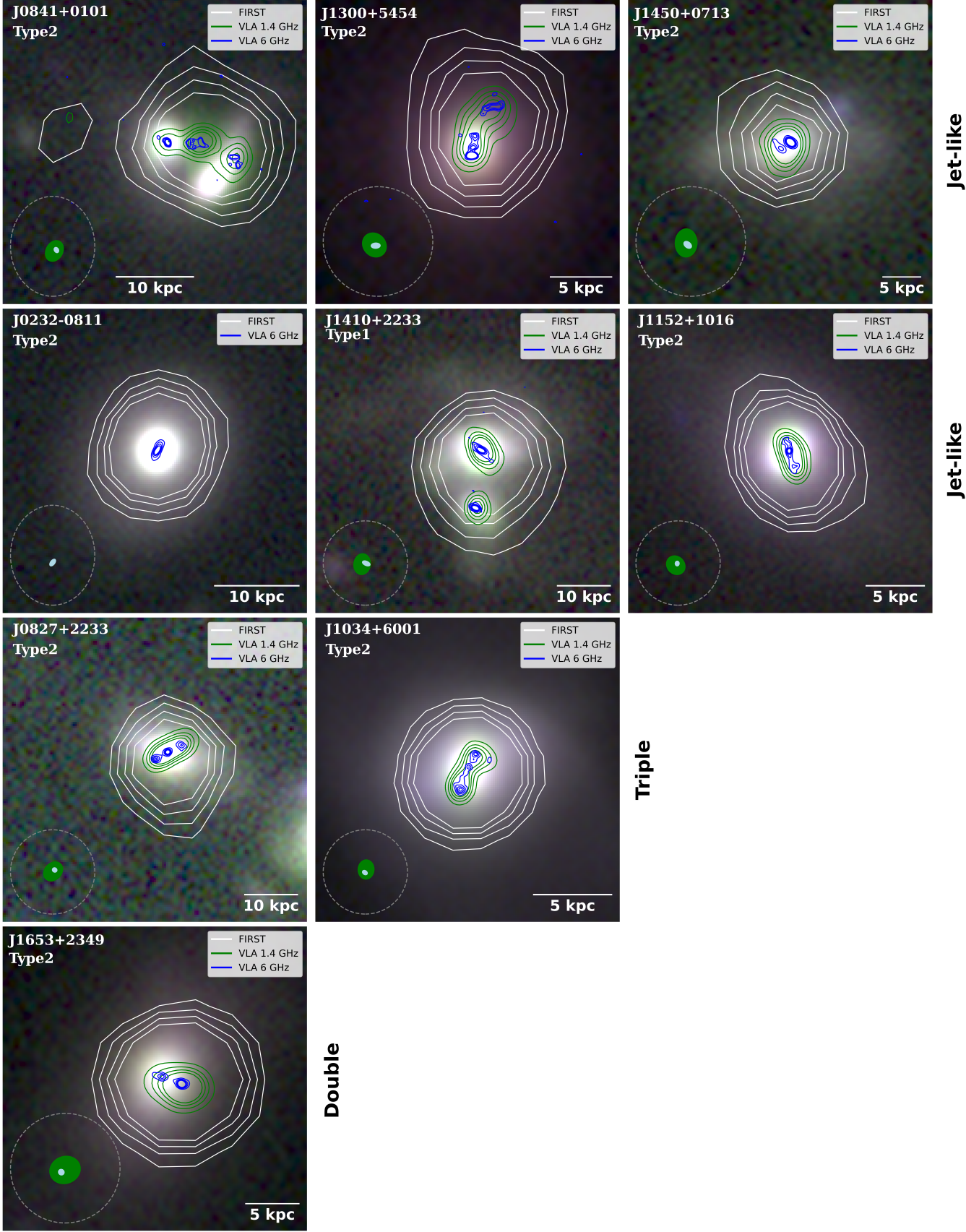


**Figure 3.** The same as Figure 2, but presenting the nine targets identified as having extended 'jet-like' structures. These targets are classified as radio-AGN based on radio morphology. We note that the target J0232–0811 was not observed in the L-band.

relevant metadata (e.g., the exact beam sizes for each map; see Data Availability section).

To extract the radio properties such as the total flux density, peak flux density, and the linear size of radio components, the targets were fitted using the `CASA` task `IMFIT`. These measured values are presented in Table 2. Where distinct multiple components were identified in an individual source, these properties have been extracted separately (i.e., those classified as doubles or triples; see Section 4.1).

We also produced spectral index ( $\alpha$ ) maps using the C-band data. We applied the two Taylor terms to model the frequency dependence of the sky emission and generated the in-band (5.25 – 7.20 GHz) spectral index maps and corresponding error maps. To extract the spectral indices of the core regions, and the associated errors, we took the median value of the  $\alpha$  image within a region that covered the core only and obtained the equivalent error from the respective error maps (see Section 4.3). These  $\alpha$  values and the corresponding errors are presented in Table 2.

## 4 RESULTS

Building on the work presented in [Jarvis et al. \(2021\)](#) and [Njeri et al. \(2025\)](#), one of the primary goals of QFeedS is to establish the fraction of moderate-to-low radio luminosity quasars (average  $\sim L_{1.4\text{GHz}} \approx 10^{23.5} \text{ W Hz}^{-1}$ ) that show radio emission associated with AGN processes. In this work, we present the results from the new QFeedS-2 sample, which comprises of 29 targets in a luminosity range of  $L_{1.4\text{GHz}} \sim 10^{22.63} - 10^{23.45} \text{ W Hz}^{-1}$ , pushing further into the radio-quiet regime than in the initial QFeedS-1 sample (see Fig. 1).

We present three sets of radio maps, those from the archival FIRST data, and our new L-band and C-band VLA maps (Section 3). Accounting for the redshift range of the sample, these maps cover a spatial resolution of  $\sim 5-20$  kpc in the 1.4 GHz FIRST images,  $\sim 1-20$  kpc in our new L-band (1.4 GHz) maps and  $\sim 0.3-1$  kpc in our new C-band (6 GHz) maps. Example maps are shown in Figure 2 and Figure 3. The measured radio properties are presented in Table 2.

In Section 4.1, we present the radio morphology classification based on visual inspection and we present the results of largest linear size (LLS) measurements in Section 4.2. In Section 4.3 and Section 4.4, we present the spectral index and brightness temperature measurements, respectively. In Section 4.5, we summarize how the radio measurements (morphology, brightness temperature and spectral index) were used for the final identification of ‘radio-AGN’.

### 4.1 Detected radio structures and their morphology

Detecting and characterising radio structures across the quasar sample provides crucial insights into the physical mechanisms driving radio emission and its potential role in feedback. Following the nomenclature used in [Jarvis et al. \(2021\)](#), we classify our targets as:

- (i) Compact (C): when only a single compact structure is identified.
- (ii) Double (D): the target has two clearly distinct radio peaks.
- (iii) Triple (T): the target has three clearly distinct radio peaks.
- (iv) Jet-like (J): when the targets show a single central radio component and are visibly spatially extended in one or two directions. In this category, we also include two sources (J0841+0101 and J1300+5454) with some more irregular structures for which two or three individual components are not well defined, but are generally collimated and jet-like.

Since the targets remained largely compact and unresolved in FIRST and only a few sources (J0841+0101, J1034+6001, J1300+5454 and J1316+4452) showed visibly extended emission

in L-band maps, we used the C-band radio maps for the radio morphology classification. There are two sources (J0213+0042 and J1410+2233) that show radio emission associated with secondary optical counterparts. Consequently, the radio structures are likely associated with companion galaxies and we ignored these radio structures in the classifications.

We find that 20/29 sources were classified as compact, with three examples shown in Figure 2. For the nine sources that show extended radio structures from the visual classification, 6/9 are classified as jet-like, 1/9 is classified as a double, and 2/9 are classified as triples. All nine of these sources are presented in Figure 3. For simplicity, and for the remainder of this work, all extended emission and well-collimated multiple components (double or triple radio peaks) are considered as jet-like (following our radio morphology classification presented in [Njeri et al. 2025](#)). However, we note that this purely defines the radio morphology and does not necessarily indicate the presence of a traditional AGN-driven jet (further discussion in Section 5.2).

In summary, a total of 9/29 targets ( $\sim 31$  per cent) show extended radio structures in the QFeedS-2 sample. This is in contrast to QFeedS-1, for which  $67^{+6.8}_{-7.6}$  per cent showed extended structures using equivalent datasets, and we discuss the variations across the whole of QFeedS further in Section 5.1 (also see similar examples from other samples in [Middelberg et al. 2007](#); [Baldi et al. 2018](#); [O’Dea & Saikia 2021](#)).

#### 4.1.1 Comparison with FIRST and implications for diffuse emission

To assess how much large-scale, low-surface-brightness radio emission might be missed by our higher-resolution L-band data, we compare the integrated flux density measured in our L-band maps with the FIRST integrated flux densities (both at 1.4 GHz). We report the per-source flux ratio:

$$R = \frac{S_{1.4\text{GHz}}}{S_{\text{FIRST}}} \quad (1)$$

in Table 2. The ratios of integrated flux between our L-band maps and FIRST range from 0.34 – 1.57 with a median value of  $\sim 1.0$ . Values of  $R < 1$  indicate cases where FIRST records more integrated flux than our high-resolution L-band maps, which is consistent with diffuse emission resolved out by the higher-resolution observations. We only find 5/26 of the sources (J1141+2156, J1410+2233, J1316+4452, J0924+1504 and J1419+1144; i.e., 19 per cent of the sample) have  $R < 1$  values ( $R = 0.34 - 0.85$ ) beyond the uncertainties. In all of these cases the  $R$  values are smaller than  $R = 1$  at a significance which is greater than three times the uncertainties. In one of these cases, J1410+2233, the difference can be attributed to the secondary optical source in the field, which contaminates the FIRST flux. Therefore, only the remaining four cases show strong evidence that  $\approx 15-66$  per cent of the 1.4 GHz flux density is resolved out in our L-band maps. These results indicate that our L-band imaging recovers the bulk of the 1.4 GHz emission measured by FIRST for the large majority of the sample.

Conversely,  $R > 1$  values indicate that our L-band maps contain more flux than measured by FIRST. This might indicate source variability between FIRST and our observations, minor variations due to slightly different frequency coverage, or other calibration and systematic errors (e.g. [de Vries et al. 2004](#); [Ofek & Frail 2011](#); [Perley & Butler 2013](#); [Mooley et al. 2016](#); [Radcliffe et al. 2019](#)). We find 8/26 sources (J0827+2233, J1110+5848, J1300+5454, J1325+1137, J1426+1040, J1426+1949, J1434+5016 and J1543+1148;  $R = 1.10 - 1.57$ ) have values of  $R > 1$  beyond the uncertainties. How-

ever, in all but two of these cases the differences are consistent with  $R > 1$  only at three times the errors. Therefore, there is only weak evidence for values of  $R > 1$  and we cannot rule out potential calibration/measurement issues. For the remaining two sources (J1426+1949 and J1543+1148, with  $R=1.57\pm0.08$  and  $R=1.30\pm0.07$ , respectively) there may have been variability of the sources between the two observing epochs at the  $\sim 30$ –60 per cent level.

We stress that additional causes, particularly time variability (FIRST epochs are typically years earlier than our new observations), different flux-extraction methods, and small frequency offsets combined with spectral curvature, can all produce deviations from  $R = 1$ . We therefore treat this comparison only as a rough indicator that, for the majority of our sources, there is not a significant fraction of large-scale gigahertz emission which is missed by our L-band VLA observations. Single-dish data or lower frequency radio observations could better quantify any additional large-scale diffuse components missed by our observations (e.g. [Condon 1992](#); [Godfrey & Shabala 2016](#); [Morabito et al. 2022](#)).

## 4.2 Largest linear sizes in the radio

To estimate the radio largest linear size (LLS) of each quasar, we used the L-band images under the assumption that the detected radio emission is fully confined within the L-band restoring beam. For compact sources, the LLS was taken directly from the deconvolved full width at half-maximum (FWHM) of the major axis returned by the two-dimensional Gaussian fitting performed with the `CASA` task `IMFIT`. These values are presented in Table 2. The quoted uncertainties correspond to the formal `IMFIT` errors on the deconvolved major axis, these incorporate the statistical uncertainties from the fit but do not explicitly propagate additional uncertainties in the restoring beam size and shape, potentially resulting in an underestimate of the true uncertainties.<sup>5</sup>

For sources exhibiting multiple components or clearly extended structures in the L-band images, we adopted the same LLS fitting procedure as [Jarvis et al. \(2021\)](#). In this approach, the LLS is defined as the projected separation between the outermost significant radio peaks. These peaks are identified in the cleaned image using intensity thresholds matched to the local rms, and their angular separation is converted to a linear scale using the source redshift. [Jarvis et al. \(2021\)](#) demonstrated that this method robustly captures the extent of jets, lobes, or knotty emission even when the morphology departs from a simple Gaussian and when individual components cannot be well-described by single-component fits. In cases where we detected a secondary radio component coincident with an optical galaxy (J0213+0042 and J1410+2233), we interpreted that component as an unrelated companion galaxy (see Section 4.1). Therefore, these secondary components were excluded from our LLS analysis.

<sup>5</sup> `CASA` `IMFIT` computes uncertainties on the deconvolved Gaussian parameters by propagating the covariance matrix of the best-fitting convolved model. The reported errors reflect statistical uncertainties from the fit (including pixel noise and parameter covariances), but they do not explicitly include systematic uncertainties due to the restoring beam model, residual calibration errors, or departures from a true Gaussian source structure. As a result, deconvolved sizes may have small formal uncertainties even when the intrinsic source size is smaller than the beam (see `CASA` Documentation: Image Analysis—`IMFIT`, `CASA` v6.5 from [CASA Team 2022](#) and [McMullin et al. 2007](#)). However, `IMFIT` will not return a size measurement if the source can not be de-convolved from the beam, and is consistent with an unresolved point source.

For the primary quasar component in these two systems, the LLS was taken from the deconvolved major-axis FWHM provided by `CASA` task `IMFIT` (as described above).

For the 3 targets (J0213+0042, J0232–0811 and J2304–0841) that were not observed in L-band, we were forced to consider the `IMFIT` deconvolved major axis in C-band as the LLS for these targets.

In Figure 4, we plot  $L_{1.4\text{GHz}}$  (derived from the NVSS measurements) as a function of the LLS for the whole QFeedS sample, where the new QFeedS-2 sample is represented with green stars, and QFeedS-1 with black stars. The LLS values of QFeedS-2 range from 0.4–6.4 kpc, with two outliers at  $\sim 0.1$  kpc (J2304–0841; but we note that this is missing the L-band data) and  $\sim 20$  kpc (J0841+0101; see Fig. 3). Our new results reveal that the gigahertz radio emission is typically compact on host galaxy scales, i.e., confined within a few kiloparsecs. Indeed, visual inspection of the radio images shows that the radio emission is confined to the spatial extent of the optical emission (with the exception of J0841+0101).

The QFeedS-2 sources have a very similar distribution of LLS sizes to the majority of QFeedS-1 (see Fig. 4). The exception is that ten (i.e., 24 per cent) of the QFeedS-1 sources have LLS values  $\gtrsim 10$  kpc, with only one source (i.e., 3 per cent) of QFeedS-2 reaching these scales. The QFeedS-1 targets with the largest sizes also tend to be those with the highest luminosities, i.e.,  $L_{1.4\text{GHz}} \gtrsim 10^{24} \text{ W Hz}^{-1}$ . We cannot rule out that even deeper radio observations would reveal lower surface brightness extended structures. However, for the majority of our sample the detected radio luminosity is dominated by the compact components recovered in our L-band maps.

This result highlights a limitation of wide, low-resolution surveys such as FIRST, with a beam of  $\sim 5''.0$ , they cannot resolve the sub-kpc to few-kpc structures revealed by higher-resolution VLA imaging. Indeed, all QFeedS-2 targets remained compact, i.e., without any visibly extended radio features in FIRST (except a marginal detection of a secondary component in J0841+0101; see top-left of Fig. 3). Our sensitive and high spatial resolution radio imaging shows that the radio emission is generally confined to the optical extent of the host galaxy, and that FIRST therefore often blends compact cores, small jets and nearby companions into a single unresolved detection. Consequently, FIRST-scale surveys do not fully characterise the key spatial scales of radio activity in these radio-quiet quasars, and, therefore sensitive sub-arcsecond imaging is required to separate compact AGN components from genuinely diffuse emission and to robustly interpret the physical origin of the radio emission. In Section 5.3 we discuss QFeedS in the context of the other AGN populations presented in Figure 4

**Table 2.** The derived radio properties for the 29 QFeedS-2 targets, including multiple radio components per source when relevant. The columns are as follows: Column (1) gives the source ID. Columns (2) and (3) give the source positions from C-band data in J2000. Columns (4–5) give the total flux density and the peak brightness from the L-band maps. Column (6) is the largest linear size, derived from the L-band; Column (7) gives the integrated flux ratios ( $R$ ) between our L-band and FIRST data; Columns (8–9) give the total flux density and peak brightness for the components observed in the C-band maps. Column (10) is the de-convolved linear size from the fits to the components observed in the C-band data (Section 3). Column (11) is the core spectral index ( $\alpha$ , over 5.25–7.20 GHz; Section 4.3). Column (12) is the brightness temperature of the cores (Section 4.4). Column (13) is the radio morphology from visual inspection (Section 4.1). Column (14) highlights the sources classified as a Radio-AGN (Section 4.5). N/O indicates that the target was not observed in L-band.

Source ID	RA	DEC	$S_{1.4\text{ GHz}}$ (mJy)	$P_{1.4\text{ GHz}}$ (mJy beam $^{-1}$ )	LLS size(kpc)	$S_{1.4\text{ GHz}}/$ $S_{\text{FIRST}}$	$S_{6.3\text{ GHz}}/$ (mJy beam $^{-1}$ )	Component (kpc)	SI	$\log(T_{\text{B}})$ (K)	Radio Morph.	Class	
(1)	(2)	(3)	(4)	(5)	(6)	(7)	(8)	(9)	(10)	(11)	(12)	(13)	(14)
J0212+0042	02:12:59.79	+00:42:26.75	N/O	N/O	N/O	N/O	0.83 $\pm$ 0.01	0.69 $\pm$ 0.01	0.54 $\pm$ 0.05	-0.71 $\pm$ 0.15	2.95	Compact	
J0232-0811	02:32:24.25	-08:11:40.19	N/O	N/O	N/O	N/O	1.14 $\pm$ 0.07	0.55 $\pm$ 0.02	1.30 $\pm$ 0.11	-1.36 $\pm$ 0.37	2.11	Jet-like	
J0827+2233	08:27:11.22	+22:33:24.21	2.48 $\pm$ 0.12	1.25 $\pm$ 0.04	6.35 $\pm$ 0.40	1.22 $\pm$ 0.10	0.27 $\pm$ 0.01	0.20 $\pm$ 0.01	5.0 $\pm$ 0.07	-2.15 $\pm$ 0.74	2.48	Triple	
	08:27:11.27	+22:33:24.76	–	–	–	–	0.25 $\pm$ 0.01	0.14 $\pm$ 0.01	0.14 $\pm$ 0.01	-0.07 $\pm$ 0.36	1.74	–	
J0841+0101	08:27:11.16	+22:33:24.64	–	–	–	–	–	0.21 $\pm$ 0.01	0.1 $\pm$ 0.02	1.12 $\pm$ 0.05	-1.15 $\pm$ 0.30	1.44	–
J0924+1504	09:24:35.35	+15:04:10.00	3.65 $\pm$ 0.58	0.68 $\pm$ 0.09	2.33 $\pm$ 0.04	1.50 $\pm$ 0.13	0.79 $\pm$ 0.03	0.65 $\pm$ 0.02	0.51 $\pm$ 0.08	0.54 $\pm$ 0.07	-0.91 $\pm$ 0.94	2.16	Jet-like
J0947+1005	09:47:33.22	+10:05:08.75	1.31 $\pm$ 0.07	1.06 $\pm$ 0.04	1.63 $\pm$ 0.36	0.93 $\pm$ 0.08	0.47 $\pm$ 0.01	0.46 $\pm$ 0.01	< 0.80	-1.15 $\pm$ 0.20	2.21	Compact	
J1034+6001	10:34:08.52	+60:01:53.00	17.60 $\pm$ 2.40	5.41 $\pm$ 0.57	3.28 $\pm$ 0.52	0.93 $\pm$ 0.13	1.72 $\pm$ 0.12	0.57 $\pm$ 0.03	2.54 $\pm$ 0.05	-1.56 $\pm$ 0.36	1.95	Triple	
	10:34:08.57	+60:01:52.159	–	–	–	–	–	0.85 $\pm$ 0.07	0.46 $\pm$ 0.03	0.32 $\pm$ 0.06	-1.36 $\pm$ 0.26	2.27	–
	10:34:08.65	+60:01:50.72	–	–	–	–	–	0.51 $\pm$ 0.01	0.39 $\pm$ 0.06	0.20 $\pm$ 0.01	-1.43 $\pm$ 0.22	2.7	–
J1110+5848	11:10:15.24	+58:48:46.02	4.61 $\pm$ 0.05	4.55 $\pm$ 0.03	0.47 $\pm$ 0.17	1.12 $\pm$ 0.06	1.46 $\pm$ 0.02	1.33 $\pm$ 0.01	0.31 $\pm$ 0.03	-1.17 $\pm$ 0.12	3.67	Compact	
J1141+2156	11:41:16.16	+21:56:21.67	0.92 $\pm$ 0.10	0.52 $\pm$ 0.04	1.53 $\pm$ 0.24	0.34 $\pm$ 0.07	0.39 $\pm$ 0.01	0.35 $\pm$ 0.01	0.14 $\pm$ 0.03	-0.86 $\pm$ 0.66	3.11	Compact	
J1152+1016	11:52:45.66	+10:16:23.83	3.50 $\pm$ 0.18	1.81 $\pm$ 0.06	2.69 $\pm$ 0.12	1.0 $\pm$ 0.06	0.44 $\pm$ 0.02	0.27 $\pm$ 0.08	0.42 $\pm$ 0.03	-1.06 $\pm$ 0.52	2.24	Jet-like	
J1203+1624	12:03:00.20	+16:24:43.72	3.01 $\pm$ 0.04	2.66 $\pm$ 0.02	1.67 $\pm$ 0.08	1.04 $\pm$ 0.05	0.83 $\pm$ 0.02	0.57 $\pm$ 0.01	0.87 $\pm$ 0.03	-1.13 $\pm$ 0.16	3.02	Compact	
J1300+5454	13:00:38.11	+54:54:36.39	2.61 $\pm$ 0.34	0.70 $\pm$ 0.07	5.64 $\pm$ 0.8	1.21 $\pm$ 0.17	0.14 $\pm$ 0.06	0.12 $\pm$ 0.01	0.24 $\pm$ 0.09	-2.61 $\pm$ 1.46	2.3	Jet-like	
J1316+4452	13:16:39.75	+44:52:35.03	3.06 $\pm$ 0.15	2.42 $\pm$ 0.07	1.02 $\pm$ 0.17	0.71 $\pm$ 0.04	0.93 $\pm$ 0.02	0.81 $\pm$ 0.01	0.34 $\pm$ 0.03	-1.13 $\pm$ 0.18	3.11	Compact	
J1325+1137	13:25:52.16	+11:37:09.79	3.14 $\pm$ 0.08	2.76 $\pm$ 0.04	1.31 $\pm$ 0.21	1.11 $\pm$ 0.05	0.79 $\pm$ 0.01	0.68 $\pm$ 0.01	0.49 $\pm$ 0.02	-0.97 $\pm$ 0.18	3.7	Compact	
J1338+503	13:38:06.53	+15:03:56.07	2.16 $\pm$ 0.04	1.93 $\pm$ 0.02	1.39 $\pm$ 0.17	0.97 $\pm$ 0.04	0.52 $\pm$ 0.01	0.38 $\pm$ 0.01	0.68 $\pm$ 0.04	-1.19 $\pm$ 0.21	2.68	Compact	
J1355+5612	13:55:16.56	+56:12:44.56	5.51 $\pm$ 0.05	5.84 $\pm$ 0.09	0.73 $\pm$ 0.16	0.97 $\pm$ 0.03	1.74 $\pm$ 0.02	1.42 $\pm$ 0.01	0.42 $\pm$ 0.02	-0.97 $\pm$ 0.12	3.4	Compact	
J1410+2233	14:10:41.51	+22:33:37.10	1.87 $\pm$ 0.09	1.16 $\pm$ 0.04	4.27 $\pm$ 0.30	0.60 $\pm$ 0.05	0.38 $\pm$ 0.02	0.23 $\pm$ 0.10	1.61 $\pm$ 0.18	-1.9 $\pm$ 0.20	1.98	Jet-like	
J1419+1144	14:19:43.79	+14:44:26.24	2.49 $\pm$ 0.04	2.26 $\pm$ 0.02	1.13 $\pm$ 0.08	0.85 $\pm$ 0.04	0.75 $\pm$ 0.02	0.52 $\pm$ 0.01	0.79 $\pm$ 0.07	-1.15 $\pm$ 0.34	2.5	Compact	
J1426+1040	14:26:14.62	+10:40:12.86	2.16 $\pm$ 0.06	1.72 $\pm$ 0.03	1.74 $\pm$ 0.20	1.10 $\pm$ 0.07	0.58 $\pm$ 0.02	0.46 $\pm$ 0.01	0.48 $\pm$ 0.08	-1.19 $\pm$ 0.27	2.62	Compact	
J1426+1949	14:26:26.93	+19:49:54.22	1.81 $\pm$ 0.03	1.66 $\pm$ 0.02	1.42 $\pm$ 0.17	1.57 $\pm$ 0.08	1.74 $\pm$ 0.01	1.66 $\pm$ 0.01	0.19 $\pm$ 0.02	-0.4 $\pm$ 0.06	4.25	Compact	
J1434+5016	14:34:11.19	+50:16:40.78	3.15 $\pm$ 0.03	2.99 $\pm$ 0.02	1.04 $\pm$ 0.09	1.14 $\pm$ 0.06	0.53 $\pm$ 0.01	0.46 $\pm$ 0.01	0.58 $\pm$ 0.03	-1.97 $\pm$ 0.37	3.41	Compact	
J1440+5303	14:40:38.20	+53:30:15.92	59.0 $\pm$ 1.20	52.05 $\pm$ 0.65	0.36 $\pm$ 0.05	1.0 $\pm$ 0.02	17.34 $\pm$ 0.45	14.81 $\pm$ 0.23	0.12 $\pm$ 0.01	-0.93 $\pm$ 0.02	4.49	Compact	
J1450+0713	14:50:34.10	+07:31:32.48	1.81 $\pm$ 0.07	1.26 $\pm$ 0.03	2.40 $\pm$ 0.29	1.06 $\pm$ 0.17	0.51 $\pm$ 0.04	0.48 $\pm$ 0.02	0.25 $\pm$ 0.22	-1.13 $\pm$ 0.45	3.38	Jet-like	
J1507+0029	15:07:19.93	+02:29:04.95	4.40 $\pm$ 0.05	4.39 $\pm$ 0.03	0.88 $\pm$ 0.08	1.0 $\pm$ 0.03	1.14 $\pm$ 0.05	0.82 $\pm$ 0.02	0.88 $\pm$ 0.08	-1.17 $\pm$ 0.28	3.35	Compact	
J1529+5616	15:29:07.45	+56:16:06.67	4.45 $\pm$ 0.14	3.90 $\pm$ 0.08	0.91 $\pm$ 0.22	1.04 $\pm$ 0.05	1.19 $\pm$ 0.03	0.9 $\pm$ 0.02	0.35 $\pm$ 0.03	-1.06 $\pm$ 0.17	2.99	Compact	
J1545+1148	15:45:03.83	+11:48:38.45	2.72 $\pm$ 0.03	2.65 $\pm$ 0.02	0.53 $\pm$ 0.11	1.30 $\pm$ 0.07	0.88 $\pm$ 0.01	0.73 $\pm$ 0.01	0.36 $\pm$ 0.14	-0.94 $\pm$ 0.17	3.18	Compact	
J1653+2349	16:53:14.99	+23:49:42.55	6.81 $\pm$ 0.31	5.14 $\pm$ 0.15	2.41 $\pm$ 0.22	0.95 $\pm$ 0.05	1.28 $\pm$ 0.06	0.90 $\pm$ 0.03	2.09 $\pm$ 0.04	-0.35 $\pm$ 0.34	3.0	Double	
J1713+5729	17:13:50.31	+57:29:54.92	7.39 $\pm$ 0.11	6.72 $\pm$ 0.06	0.85 $\pm$ 0.12	1.0 $\pm$ 0.02	1.74 $\pm$ 0.03	1.60 $\pm$ 0.02	0.27 $\pm$ 0.05	-1.34 $\pm$ 0.19	3.77	Compact	
J2304-0841	23:04:43.48	-08:41:08.65	N/O	N/O	N/O	N/O	13.25 $\pm$ 0.23	12.88 $\pm$ 0.13	0.06 $\pm$ 0.02	0.64 $\pm$ 0.02	5.3	Compact	
												R-AGN	

### 4.3 Spectral Indices

Spectral indices provide a powerful diagnostic tool for identifying AGN cores, lobes, jets, and studying AGN feedback and lifecycles (e.g. Laing & Peacock 1980; Begelman et al. 1984; Hardcastle & Croston 2020; Harwood et al. 2022). Extragalactic radio sources follow the power-law spectra where the observed flux density follows  $S_\nu \propto \nu^\alpha$ . A flat or inverted spectrum  $\alpha \geq -0.5$  is indicative of an AGN core and a steep spectrum  $-0.5 \leq \alpha \leq -2$  is indicative of large scale emission from processes such as jets, lobes, shocks from outflows and diffuse emission from star formation.

We measured the spectral index of radio cores identified in our C-band radio maps (5.25 – 7.20 GHz; see Section 3). For the multi-component sources, the brightest radio peak was taken to be the core (although not necessarily a true ‘core’). The spectral indices are listed in Table 2 and are presented in Figure 5.

Only 3/29 (J1426+1949, J1653+2349 and J2304–0841), i.e., 10 per cent, of the QFeedS-2 targets show a flat spectrum ( $\alpha \geq -0.5$ ). In comparison, 7/42 showed a flat spectrum (i.e., 17 per cent) in the QFeedS-1 sample (Jarvis et al. 2021). Overall, only a minority of the sources (14 per cent) across the whole of QFeedS show flat or inverted cores (see Fig. 5). Indeed, the majority show very steep spectra with values around  $-1$ . The relevance of these measurements across the combined samples is discussed further in Section 5.1.

### 4.4 Brightness temperature

Brightness temperature ( $T_B$ ) is defined as the temperature of a black-body that would produce the observed radio surface brightness (flux density per solid angle) at the given frequency (e.g. Morabito et al. 2022). In practice,  $T_B$  serves as a proxy for radio surface brightness, whereby compact, synchrotron-emitting AGN cores (the bases of jets) often show very high  $T_B$  because a large flux density is concentrated into a very small solid angle. By contrast, purely star-forming regions have a physical limit on the radio surface brightness they can produce. In fact, models of compact starbursts predict an upper bound of order  $T_B \sim 10^5$  K even in the most extreme systems (Condon 1992). Thus, any unresolved radio core with a measured  $T_B$  above this starburst limit is a strong indicator of AGN activity.

To derive the brightness temperatures, we use our measurements from the high-resolution C-band data ( $\theta_{\text{res}} \sim 0''.3$ ) and apply the standard equation (e.g. Condon et al. 1982; Ulvestad et al. 2005; Njeri et al. 2025), following:

$$T_B = 1.22 \times 10^{12} (1+z) \left( \frac{S_\nu}{1 \text{ Jy}} \right) \left( \frac{\nu}{1 \text{ GHz}} \right)^{-2} \left( \frac{\theta_{\text{maj}} \theta_{\text{min}}}{1 \text{ mas}^2} \right)^{-1} \text{ K}, \quad (2)$$

where  $\theta_{\text{maj}}$  and  $\theta_{\text{min}}$  are the deconvolved major and minor axes from the elliptical Gaussian model,  $S_\nu$  is the observed peak flux density, and  $\nu$  is the observing frequency. As noted by Morabito et al. (2022), this means  $T_B$  depends inversely on the observing frequency and beam size: at lower frequencies or higher resolution, the same flux density corresponds to a higher  $T_B$ . Using our  $\sim 0''.3$  beam at  $\sim 6$  GHz (Equation 2), we derive  $T_B$  for each source. These values are presented in Figure 5 and are tabulated in Table 2.

To distinguish AGN from star-formation, we adopt the same criteria used by Jarvis et al. (2021), namely  $T_B > 10^{4.6}$  K. Jarvis et al. derive this threshold by scaling the Condon et al. (1991) starburst limit to C-band. At our central frequency of  $\sim 6$  GHz and redshift ( $z \sim 0.1$ ), starbursts are not expected to exceed this value, so any brighter core is expected to be AGN-dominated. The  $T_B$  values for the QFeedS-2 sample range from  $1.3 \times 10^2$  –  $2.0 \times 10^5$  K, with only one target (i.e.,  $\sim 3$  per cent), J2304–0841, meeting this criterion (see

Fig. 5). For comparison, about  $\sim 17$  per cent of the QFeedS-1 cores exceed  $10^{4.6}$  K (black stars in Fig. 5), reflecting that those sources are on average more radio-luminous and host more compact, high  $T_B$  cores.

It is important to note that  $T_B$  is a very conservative radio-AGN diagnostic and a measurement below  $T_B < 10^{4.6}$  K does not prove the absence of a radio emission associated with AGN. Many QFeedS-2 sources have lower peak fluxes and slightly resolved low-surface brightness cores, which lead to beam dilution and thus could underestimate the  $T_B$  measurements. Additionally,  $T_B$  measurements depend strongly on the resolution and can underestimate  $T_B$  for extended or partially resolved sources, potentially missing the weaker AGN cores (e.g. Radcliffe et al. 2018; Morabito et al. 2022; Njeri et al. 2023, 2025; Morabito et al. 2025b). Indeed, high spatial resolution and high sensitive radio imaging can be more effective at isolating true AGN cores, with high  $T_B$ , from dilution from other processes (see discussion of QFeedS-1 using higher resolution radio data in Njeri et al. 2025). In general, one can only securely classify a source as AGN if  $T_B$  exceeds the starburst limit (e.g. Kewley et al. 2000). If  $T_B$  is below the limit, the source may still host an AGN core, but any bright AGN contribution would need confirmation via other means (see ‘AGN/SF’ region in Fig. 5). For this reason, we use  $T_B$  as one diagnostic among several. As in previous work, we supplement this diagnostic with spectral index and morphology diagnostics to identify AGN-related radio emission (Jarvis et al. 2019; Njeri et al. 2025). As discussed in the following sub-section, this multi-criteria approach, is essential for identifying radio emission associated with AGN.

### 4.5 Radio-AGN identification

No QFeedS-2 target is classified as ‘radio loud’ based either on their radio to [O III] luminosities (applicable for all sources) or radio to optical continuum luminosities (applicable for the Type 1 sources; see Section 2.3). Radio-quiet quasars exhibit radio luminosities that are orders of magnitude fainter than their radio-loud counterparts, typically in the range  $L_{1.4 \text{ GHz}} \sim 10^{21-25} \text{ W Hz}^{-1}$  (Zakamska et al. 2004; Padovani 2016). These faint signals are easily lost due to sensitivity limitations, or could be overwhelmed by star formation contributions, especially in shallow or low-resolution surveys such as NVSS or FIRST. Thus detecting and characterising radio emission from radio-quiet quasars is extremely challenging. Using sensitive high-resolution radio imaging obtained in this work, we probed for the presence of radio emission associated with AGN based on the radio morphology (Section 4.1), the spectral index (Section 4.3) and the brightness temperature (Section 4.4):

i) Radio morphology: high resolution radio imaging can identify structures on a few kiloparsec to sub-kiloparsec scales. Elongated emission, double-lobed structures, well-collimated multiple components and linear features extending from a central source are indicative of low-power AGN jets, possibly compact due to confinement or young age, or from shocks caused by quasar winds (e.g. Nims et al. 2015; Baldi et al. 2021; Njeri et al. 2025). Nine targets (i.e.,  $\sim 31$  per cent) show such morphologies (see Fig. 3) and are therefore classified as radio-AGN.

ii) Spectral indices: our high resolution radio imaging enabled us to identify compact nuclear components of these radio-quiet quasars targets. Three targets (J1426+1949, J1653+2349 and J2304–0841; i.e.,  $\sim 10$  per cent) show a flat spectrum ( $\alpha \geq -0.5$ ), which is likely indicative of an AGN ‘core’, and are therefore classified as radio-

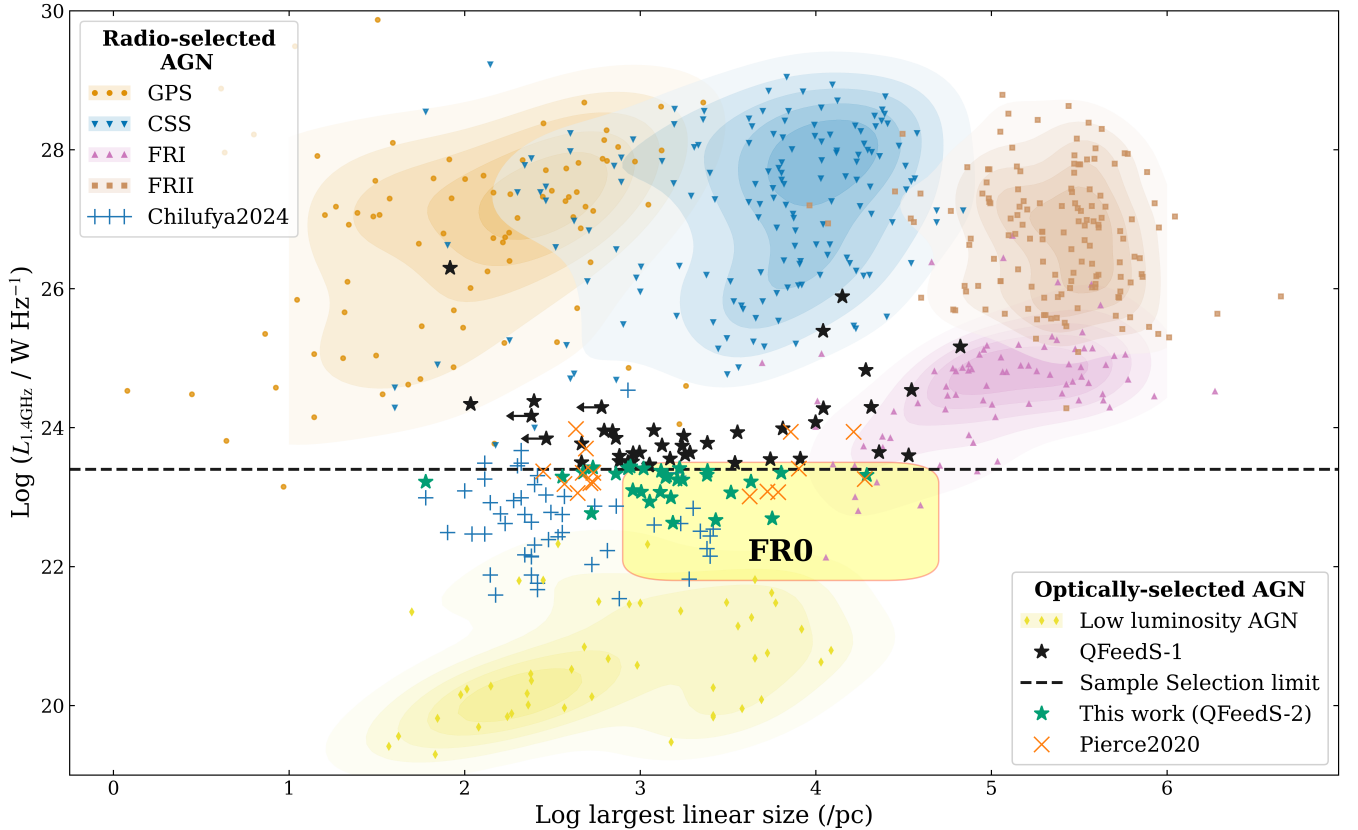


**Figure 4.** Radio size versus radio luminosity for the QFeedS quasars compared to classical radio-selected AGN populations. Coloured points and contours mark the loci of GPS, CSS, FRI and FRII sources, while the shaded yellow region highlights the FR0 domain as defined in Baldi (2023). Black stars show the QFeedS-1 sample (Jarvis et al. 2021), and green stars show the new QFeedS-2 sample presented in this work. The dashed line marks the QFeedS-1 radio luminosity selection limit. The majority of QFeedS-2 remain compact at sub-arcsecond to arcsecond scales ( $\sim 3$  kpc), and broadly consistent with FR0-like systems. This distribution closely parallels the compact steep-spectrum sources reported in Chilufya et al. (2024) (plus symbols), though QFeedS quasars are optically selected and radiatively efficient, in contrast to many radio-selected samples. By contrast, QFeedS-1 shows a higher fraction of extended sources with higher radio luminosities, bridging towards CSS and FRI-like populations. At the same time, the QFeedS-2 sample overlaps in luminosity with the intermediate-power HERGs of Pierce et al. (2020) (cross symbols), but stands out for its strong [O III] emission despite compact radio morphologies. Taken together, QFeedS maps a broad continuum of radio properties in optically-selected quasars and highlights the role of QFeedS in connecting low-luminosity FR0-like AGN with the more extended radio populations, while demonstrating the diversity of radio output among radiatively-efficient quasars across several orders of magnitude in  $L_{1.4\text{GHz}}$ .

AGN. One of these sources, J1653+2349, is already considered a radio-AGN based on morphology.

iii) Brightness temperature ( $T_B$ ): high  $T_B$  values are inconsistent with star formation and point to synchrotron emission from an AGN core (e.g., Condon 1992). A compact unresolved radio core at sub-arcsecond ( $< 0''.3$ ) scales with high  $T_B > 10^{4.6}$  K is indicative of radio AGN. Only one target (J2304-0841; i.e.,  $\sim 3$  per cent) has  $T_B > 10^{4.6}$  K. This target was already considered a radio-AGN based on a flat spectral index.

Overall, 11/29 targets ( $\sim 38$  per cent) of QFeedS-2 are classified as radio-AGN using the combined criteria of radio morphology, spectral index and brightness temperature. However, the origin of radio emission in the remaining 18/29 ( $\sim 62$  per cent) remains uncertain, largely due to our radio data limitations and a lack of complementary multi-wavelength data, particularly in the far infrared. For example, with far infrared emission we could assess if the radio luminosity is above that expected from star formation following the far-infrared radio correlation of star-forming galaxies (e.g. Del Moro et al. 2013; Delhaize et al. 2017; Jarvis et al. 2021; Eberhard et al. 2025; Wang et al. 2024, also see Section 5.2.1). Therefore, we consider the 38 per cent

of radio-identified AGN in QFeedS-2 to be a lower limit of the true fraction.

## 5 DISCUSSION

The full Quasar Feedback Survey (QFeedS), comprises of 71 optically selected,  $z < 0.2$  quasars (Section 2.2). Combining the initial QFeedS-1 sample (Jarvis et al. 2021) and QFeedS-2 sample (this work), this spans an extensive radio luminosity range from  $L_{1.4\text{GHz}} = 10^{22.6} - 10^{26.3} \text{ W Hz}^{-1}$ , encompassing nearly four orders of magnitude. The QFeedS-1 sample, covers the higher luminosities, with a radio luminosity range of  $L_{1.4\text{GHz}} = 10^{23.45} - 10^{26.30} \text{ W Hz}^{-1}$  and a median of  $\sim 10^{23.8} \text{ W Hz}^{-1}$ , while the low luminosity QFeedS-2 sample has a radio luminosity range of  $L_{1.4\text{GHz}} = 10^{22.63} - 10^{23.44} \text{ W Hz}^{-1}$ , and a median of  $\sim 10^{23.29} \text{ W Hz}^{-1}$ .

This combined sample enables a rare opportunity to systematically study how the radio emission in quasars evolves with radio luminosity, and obtain more insight into feedback processes in a representative quasar sample. Here we discuss the radio AGN identification across the full QFeedS sample (Section 5.1), before exploring more

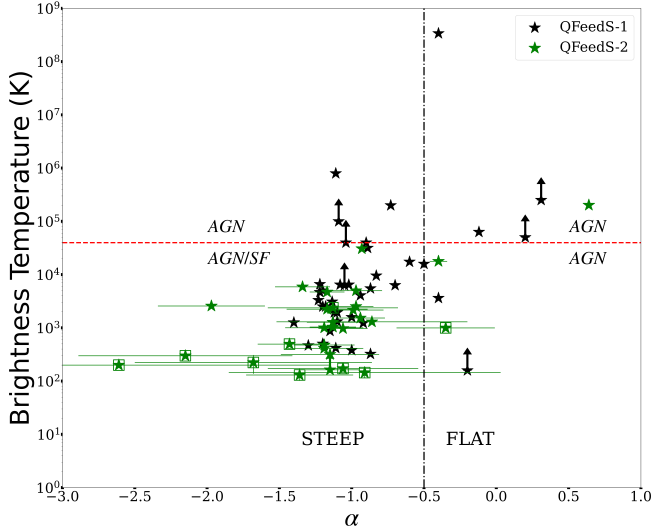


**Figure 5.** Brightness temperature ( $T_B$ ) as a function of spectral index,  $\alpha$ , ( $\sim 5$ – $7$  GHz) for the whole Quasar Feedback Survey sample. Black stars highlight the QFeedS-1 sample of 42 targets as presented in Jarvis et al. (2021). The new sample of 29 targets presented in this work (QFeedS-2) is highlighted by green stars. For the multi-component sources, we plotted the component with the highest  $T_B$  value. The dashed red line highlights the lower limit of brightness temperature  $T_B = 10^{4.6}$  K for selected radio AGN. The vertical dot-dashed line separates flat and steep sources. For sources in the bottom-left quadrant, these radio measurements can not distinguish between AGN and star formation (SF). However, the targets highlighted by green squares indicate the QFeedS-2 sources that were classified as radio-AGN based on their morphology (Section 4.1).

deeply the potential origins of the radio emission (Section 5.2), and comparing to other AGN populations (Section 5.3).

### 5.1 Radio-AGN identification in the full QFeedS sample

In Figure 5, we summarise the radio-AGN selection criteria used in this work for QFeedS-2 (green stars), which are: (1) morphology (highlighted with squares; 9 targets, i.e., 31 per cent); (2) flat core spectral indices of  $\alpha > -0.5$  (right of dot-dashed line; 3 targets, i.e., 10 per cent); and, (3) high brightness temperature measurements (above horizontal dashed line; 1 target, i.e., 3 per cent). Based on these combined criteria, 11/29 (38 per cent) of sources are classified as radio-AGN in QFeedS-2. In the same figure we show QFeedS-1 (black stars), which show a higher incidence of flat spectral indices ( $17^{+6.5}_{-5.0}$  per cent, compared to  $10^{+7.0}_{-4.4}$  per cent in QFeedS-2) and high brightness temperatures ( $17^{+6.5}_{-5.0}$  per cent compared to  $3^{+5.2}_{-2.1}$  per cent in QFeedS-2).

Following the same radio morphology criteria applied in this work (i.e., sources with double, triple, or jet-like morphologies),  $55^{+7.5}_{-7.7}$  per cent<sup>6</sup> of targets in the QFeedS-1 sample are classified

<sup>6</sup> We note that 67 per cent of sources in Jarvis et al. (2021) are described as having extended structures. However, excluding sources showing diffuse/irregular morphologies, only 55 per cent of the sample is classified as radio-AGN based on morphology alone. We also note that Jarvis et al. (2021) quoted a lower fraction of  $\sim 16$  per cent based on much stricter morphology criteria; however, here we apply a looser criteria, following Njeri et al. (2025), and note that sources not classified as radio-AGN based on morphology in Jarvis et al. (2021), are identified as radio-AGN based on other diagnostics, reassuring us that this is a reasonable approach.

as radio-AGN based on radio morphology alone, compared to  $31^{+9.1}_{-7.8}$  per cent in QFeedS-2. These fractions of identified AGN-like morphologies are broadly consistent with results for comparable samples at similar luminosities and redshifts (see Section 5.3). The QFeedS-1 sources span radio sizes of  $\sim 0.1$  –  $67$  kpc (Jarvis et al. 2021), while QFeedS-2 sizes range  $\sim 0.1$  –  $20$  kpc (see Fig. 4). Most objects in both samples have radio emission confined to host-galaxy scales (i.e.,  $\leq$  a few kpc), although a minority of QFeedS-1 sources and one QFeedS-2 target exhibit substantially larger sizes (see Section 4.2). Importantly, this size distribution masks a wide variety of radio morphologies, and even though the targets were selected to have similar [O III] luminosities, we observe compact unresolved cores, small jets, hotspots and diffuse structures across the whole sample (Figs. 2 – 3).

Using the consistent and combined three criteria of radio morphology, brightness temperature and spectral indices, we identify 28/42 ( $67^{+6.8}_{-7.6}$  per cent) and 11/29 ( $38^{+9.3}_{-8.5}$  per cent) sources as radio-AGN across QFeedS-1 and QFeedS-2, respectively. However, it is already known that additional information can identify more radio-AGN, and these are likely lower limits of the true fractions. For example, using sufficiently high quality far-infrared measurements, that were available for a sub-set of the sample, Jarvis et al. (2021) found another 12 per cent of QFeedS-1 quasars to be classified as radio-AGN solely based on radio-excess measurements (following e.g., Condon 1992; Helou et al. 1985; Del Moro et al. 2013; Marvil et al. 2015), i.e., where their radio morphology, spectral indices and brightness temperature criteria were inadequate (see Fig. 6 in Jarvis et al. 2021). Sufficient quality far-infrared data are not available for QFeedS-2 for a comparable analysis; however, we briefly investigate the likely contribution of star formation in Section 5.2.1. Overall, this highlights the need for high resolution multi-band radio imaging combined with multi-wavelength information, particularly infrared, as we push further into the radio-quiet regime (also see e.g., Hardcastle et al. 2025).

In Figure 6 we present a summary of the radio-AGN identification approaches across the whole QFeedS sample, in the form of spectral index versus radio luminosity diagram<sup>7</sup>. Unsurprisingly, for the moderate radio luminosities covered by the QFeedS quasars, only a minority of the sample have strong radio-AGN cores based on our VLA data, as indicated by flat spectral indices or high brightness temperatures. However, as expected, this fraction increases as a function of radio luminosity. On the other hand, radio morphology results in a higher fraction of radio-AGN being identified in QFeedS, which is only possible thanks to our high resolution radio maps.

Higher-resolution follow-up of QFeedS-2 is needed because a substantial fraction of the radio power in these quasars appears to arise on sub-kiloparsec scales (i.e.,  $\leq 1$  kpc to a few hundred parsecs; e.g., Njeri et al. 2025). Compact cores, frustrated jets, hotspot knots and shocked regions can all be concentrated within these small spatial extents and therefore remain unresolved or beam-diluted in our VLA maps. Observations with finer angular resolution (e.g., *e*-MERLIN at  $\leq 100$  pc scales or VLBI at parsec scales) both increase brightness temperature sensitivity and resolve compact AGN features, often revealing AGN signatures missed at lower resolution. For example, 6 GHz *e*-MERLIN imaging of the QFeedS-1 sample at  $\leq 100$  pc resolution increases the fraction of sources confidently classified as

<sup>7</sup> One QFeedS-1 target (J1016+0028) is absent from Figure 6 due to the lack of a core spectral index measurement, as it was undetected in the C-band data (Jarvis et al. 2021). Nevertheless, we note that the source was classified as a radio-AGN based on its morphology.

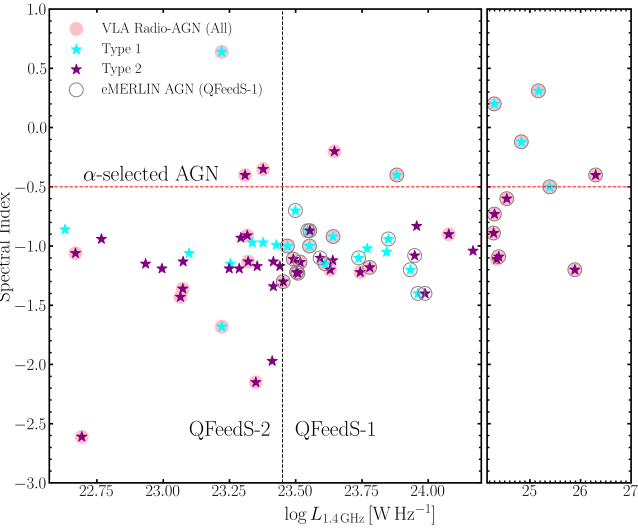


**Figure 6.** Core spectral index ( $\sim 5$ – $7$  GHz) versus  $1.4$  GHz (NVSS) radio luminosity for the QFeedS sample. The vertical dashed line separates QFeedS-1 from QFeedS-2 sources. The plot is split into two panels, covering different luminosity ranges for more clarity over the wide parameter space. Cyan stars denote Type 1 quasars and purple stars denote Type 2 quasars. Solid circles highlight quasars identified as radio-AGN based on the criteria used in this work. Both sub-samples are dominated by steep spectrum emission; however, flatter-spectrum sources are more common at higher luminosities (QFeedS-1), for the Type 1 quasars, consistent with an increased contribution from compact AGN-related cores. Open circles mark QFeedS-1 sources identified as radio-AGN based on follow-up higher resolution *e*-MERLIN radio imaging.

radio-AGN to nearly 90 per cent (see open circles in Fig. 6), compared with 60 per cent identified from low resolution data (Njeri et al. 2025). Higher-resolution observations of QFeedS-2 are likely to uncover additional compact AGN components and to provide a more complete census of radio-AGN across the full QFeedS luminosity range.

### 5.1.1 Type 1 versus Type 2 quasars

Since our sample is composed of  $\sim 35$  per cent Type 1 and  $\sim 65$  per cent Type 2 quasars, we briefly investigate the radio properties across the two classes of AGN in our QFeedS sample. The division of sources into optical Type 1 (cyan stars) and Type 2 (purple stars) in Figure 6 shows no strong offset in spectral index distribution between the two classes. The exception is for the highest radio luminosities ( $\gtrsim 10^{24}$   $\text{W Hz}^{-1}$ ), where the Type 1 systematically have flatter spectral indices. We also note that the extended AGN-like morphologies are more frequently identified in Type 2 sources, with  $\sim 52$  per cent compared to only  $\sim 32$  per cent for the Type 1. These trends, albeit weak, may reflect observational biases in detecting compact cores against different host galaxy environments (Zakamska et al. 2016; Villar Martín et al. 2021), and are broadly consistent with an orientation-based model. Specifically, for a more directly face on view for Type 1 quasars, we would expect the radio emission to be more dominated by the radio core (with compact, flat spectrum emission).

## 5.2 Potential origin of the Radio Emission

For  $\sim 60\%$  of our QFeedS-2 sample, which covers the modest radio luminosities ( $L_{1.4 \text{ GHz}} \sim 10^{22.63} - 10^{23.45} \text{ W Hz}^{-1}$ ), the origin of the

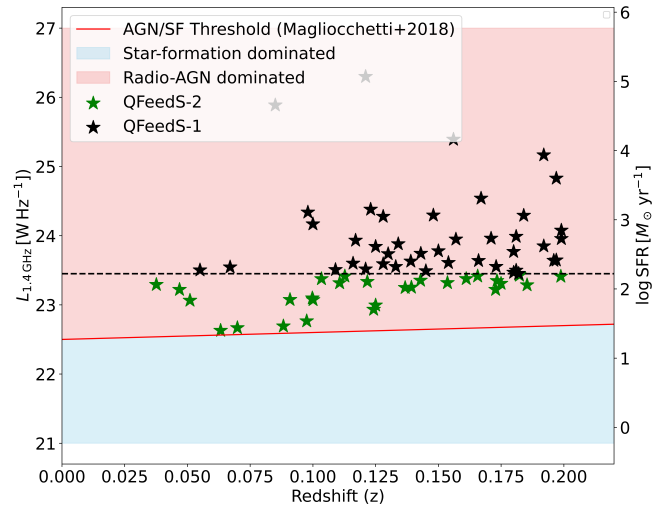


**Figure 7.** Radio luminosity at  $1.4$  GHz (NVSS) versus redshift for QFeedS quasars and the corresponding star-formation rates as derived from the standard star-formation rate calibrators, is shown on the right axis (see Section 5.2.1). Black stars represent QFeedS-1 and green stars represent QFeedS-2. The solid red line shows the AGN / star formation threshold for the galaxy population from Magliocchetti et al. (2018), separating the star-formation dominated (blue shaded) and radio-AGN dominated (pink shaded) regimes. The dashed black line marks the QFeedS-1/QFeedS-2 selection limit. Most QFeedS quasars, particularly the luminous QFeedS-1, lie firmly above the star-forming locus, indicating that their radio emission is most likely dominated by AGN processes rather than star formation. The lower-luminosity QFeedS-2 source scatter closer to the threshold but still occupy predominantly AGN-dominated space.

radio emission remains ambiguous. Although we lack the diagnostics to definitively rule out star formation in individual targets, here we briefly assess the likelihood that star formation is a dominantly contributing factor across the QFeedS sample as a whole.

### 5.2.1 Star formation versus radio-quiet AGN

Single-band radio conversions have been used to convert radio luminosity into star formation rates for star-forming galaxies (e.g., Yun et al. 2001; Murphy et al. 2011; Kennicutt & Evans 2012). Compact, low-power jets, wind-ISM shocks, and coronal synchrotron all produce steep-spectrum emission that masquerades as star formation when using single-band radio calibrations. Therefore, when AGN may be present these calibrations would only provide upper limits on star-formation rate measurements (e.g. Yun et al. 2001; Del Moro et al. 2013; Padovani 2017). Based on large sample studies, at  $L_{1.4 \text{ GHz}} \approx 10^{23} \text{ W Hz}^{-1}$ , the radio emission in quasars increasingly overlaps the regime of star-forming galaxies, with non star-forming processes easily supplying a large fraction of the radio power. We place our QFeedS sample into the context of such studies, assessing the likely contribution from star formation to the sample as a whole.

In Figure 7 we present radio luminosity as a function of redshift for the combined QFeedS samples. As a rough estimate, on the right-hand axis, we convert these radio luminosities into star-formation rates, assuming a 100% contribution from star formation to the radio emission and averaging multiple conversion calibrations (Yun et al. 2001; Murphy et al. 2011; Kennicutt & Evans 2012). The inferred star formation rates range from  $\sim 30 \text{ M}_\odot \text{ yr}^{-1}$  to  $\sim 10^5 \text{ M}_\odot \text{ yr}^{-1}$ . For context, the typical star-formation rates of radiatively-luminous AGN at  $z \sim 0$  are found to be  $0.1$ – $50 \text{ M}_\odot \text{ yr}^{-1}$  (e.g., Zakamska

et al. 2016; Shimizu et al. 2017; Jarvis et al. 2019; Jackson et al. 2020). Using this conversion, we find that 67/71 (94 per cent) of the inferred star-formation rates are greater than  $50 \text{ M}_\odot \text{ yr}^{-1}$ , which is an uncomfortably high value for these very low redshift quasars. Therefore, it is most likely that there is a significant contribution to the radio emission from AGN for the majority of the sample. Indeed, these standard single-band calibrations yield implausibly high star-formation rates in AGN hosts due to contamination from compact synchrotron processes. The inflated inferred star-formation rate values we measure are consistent with previous works that report radio-based star-formation rates in quasars and radio-quiet AGN tend to overshoot far-infrared or spectral energy distribution based estimates due to contamination from low-power jets, coronal activity, and wind-driven shocks (e.g. Del Moro et al. 2013; Behar et al. 2015; Zakamska et al. 2016; Delvecchio et al. 2017; Padovani 2017; Smolčić et al. 2017; Bernhard et al. 2022; Liao et al. 2024; Calistro Rivera et al. 2024).

We further compare to the redshift-dependent separation between star-formation dominated and AGN-dominated radio luminosity regimes as derived by Magliocchetti et al. (2018), which is represented by the solid red curve in Figure 7. The QFeedS-1 quasars, at higher radio luminosities, sit firmly within the AGN-dominated region, consistent with their high fraction of radio AGN identification from other methods (Jarvis et al. 2021; Njeri et al. 2025). In contrast, QFeedS-2 sources cluster closer to the threshold, with some appearing near the boundary between the two regimes; however, still within the AGN-dominated regime.

Although we can not rule out a significant contribution from star formation in all individual sources, we conclude that the QFeedS quasars, which are preselected as luminous [OIII] and radio detected in FIRST, are likely to have their radio emission predominantly associated with AGN related processes. This supports the idea of an increasing body of work implying a significant contribution of AGN-related emission to the radio output of radio-quiet quasars (e.g., Zakamska et al. 2016; White et al. 2017; Panessa et al. 2019).

### 5.2.2 Jets and winds in radio-quiet quasars

At the high-luminosity end (QFeedS-1), the radio emission is often clearly AGN-dominated, with compact jet-like morphologies, flat to moderate spectral indices and high brightness temperatures ( $T_B \geq 10^{4.6} \text{ K}$ ), pointing to relativistic jet activity as the primary driver, although shocks due to quasar-driven winds can not be ruled out in all cases (Jarvis et al. 2021). These sources align with classical radio-intermediate and radio-loud quasars, where radio-AGN activity is well established (Jarvis et al. 2021; Njeri et al. 2025).

Interestingly, the majority of QFeedS sources show very steep spectral indices of  $\approx -1$  (Fig. 6). Such a steep spectral slope could be an indication of shocks due to quasar driven winds and/or low power radio jets interacting with the ISM (e.g., O'Dea 1998; Nims et al. 2015; Fawcett et al. 2025). Indeed, spatially-resolved multi-wavelength analysis of subsets of the QFeedS-1 sample show a high incidence of interaction with the ISM (e.g., Jarvis et al. 2019; Girdhar et al. 2022, 2024). However, distinguishing between jets and winds as the origin of the radio emission in AGN-dominated systems, is very challenging. Whilst spatially-resolved polarisation-sensitive observations may provide some diagnostics, sensitivity-limited imaging alone can be expected to remain ambiguous based on simulations (e.g., Meenakshi et al. 2024). Nonetheless, in sources where 'AGN-like' (extended) morphologies are observed in QFeedS-2 (see Fig. 3), we discuss their morphologies below, in the context of previous observations.

The jet-like feature in J0841+0101 appears to be bipolar with an end-to-end extent of nearly 20 kpc. It is important to note the filamentary nature of the jet and its western end lying close to the neighboring galaxy (but not coincident with its optical center). On the eastern end, only a single radio feature is observed, and only in the L-band data. The jet-like features in J1300+5454, J1034+6001, J0827+2233, and J1152+1016 display morphologies similar to those observed in jetted radio-loud AGN except for the fact that these jets are much smaller in extent. J1300+5454, J1034+6001 and J0827+2233 appear to show terminal hotspots like FRII radio galaxies, while the jet in J1152+1016 shows an S-shaped FRI-like morphology. The more compact extensions in J0232-0811 and J1410+2233 resemble similar extensions observed in Seyfert galaxies and other radio-quiet quasars (e.g., Rao et al. 2023; Silpa et al. 2023). The radio structures in J1450+0713 and J1653+2349 resemble a core-hotspot-like structure but the counter-hotspot is not clearly visible. For all radio sources that are compact (Fig. 2), it is possible that jets exist on even smaller sub-kpc scales that would need sub-arcsecond or VLBI observations to resolve (e.g., Kharb et al. 2019, 2021; Njeri et al. 2025).

Taken together, these diverse jet-like morphologies illustrate that even within radio-quiet quasars, small-scale jets and compact outflows significantly impact the observed radio emission. Although much smaller than classical FR I/II radio galaxies (Fig. 4), the presence of hotspots, bends, and filamentary features strongly suggests jet-ISM interactions, rather than star-formation origins (e.g. Baldi et al. 2018; Jarvis et al. 2019; Rosario et al. 2020). At the same time, the coexistence of compact, steep-spectrum sources without obvious extended features highlights that multiple mechanisms, ranging from low-power or frustrated jets, coronal emission and outflow-driven shocks, likely contribute across the QFeedS population (e.g. Laor & Behar 2008; Panessa et al. 2019; Silpa et al. 2023). Thus, the radio emission in these quasars is unlikely to be ascribed to a single origin. Instead, it reflects a continuum of AGN-driven processes operating over different spatial and energetic scales, potentially intertwined with the dynamical state of the host galaxy (e.g. Padovani 2017; Hardcastle & Croston 2020).

### 5.3 Comparison to other AGN samples

Compact, low-luminosity radio-AGN often exhibit steep spectra and show jet-like structures on kiloparsec (or smaller) scales, if spatially resolved (see review by Baldi 2023). For QFeedS-2, 26/29 sources show steep spectra  $\alpha < -0.5$  (Fig. 5), consistent with optically thin synchrotron emission. However, since nearly all remain compact on kiloparsec scales, this compactness likely reflects low-power or frustrated jets, or shocks from quasar-driven winds, confined to small spatial scales (e.g. Baldi et al. 2015; Silpa et al. 2020; Baldi 2023; Njeri et al. 2025, Section 5.2.1). As shown in Figure 4, the QFeedS quasars have radio sizes overlapping Compact Steep Spectrum (CSS) and low-size end of FRI sources. Strikingly,  $\sim 80$  per cent of the QFeedS-2 sources cluster in the same region as FRI galaxies (Fig. 4; yellow shaded region), which is traditionally associated with low-accretion radio galaxies (Baldi 2023). However, the high [O III] luminosities of our sample indicate radiatively efficient quasars, illustrating a decoupling between radiative accretion power and observed radio luminosities and sizes.

The compact, low-luminosity objects in QFeedS may also represent early evolutionary stages of Gigahertz Peaked Spectrum (GPS) and Compact Steep Spectrum (CSS) sources, in which jets remain confined within their host galaxies (particularly for the QFeedS-1 sample; see more discussion in Njeri et al. 2025). Kunert-

Bajraszewska et al. (2010) proposed that such low-luminosity compact systems could be young radio sources that later evolve into CSS of FRI galaxies, while Slob et al. (2022) similarly identified compact peaked-spectrum sources in LOFAR consistent with either young or confined jets.

Recent low-redshift studies provide additional insights into the low-luminosity compact radio AGN population. For instance, Pierce et al. (2020) analysed intermediate-power high excitation radio galaxies (HERGs;  $22.5 < \log L_{1.4\text{GHz}} < 24.0 \text{ W Hz}^{-1}$ ) at  $z < 0.1$  and found a lower incidence of extended radio morphologies, steep-spectrum compact sources in the less powerful half of their sample, compared to classical radio galaxies (see crosses in Fig. 4). This may suggest that the low-power AGN can persist in relatively undisturbed systems, contrasting with the merger-driven environments of more powerful radio AGN. The QFeedS-2 sample, while overlapping in radio luminosity with these HERGs, they differ in that they are preselected as luminous [O III] quasars, pointing to strong radiative accretion event with radio output that is relatively compact and weak.

Similarly, Chilufya et al. (2024) studied LOFAR-selected low-luminosity ( $L_{150\text{MHz}} < 10^{25} \text{ W Hz}^{-1}$ ) radio-AGN at  $0.03 < z < 0.1$  and reported that most sources are unresolved at sub-kpc scales, and often have steep-spectrum, strongly resembling CSS, GPS and FR0-like systems (see plus symbols in Fig. 4). This is directly comparable to the QFeedS-2 sources, which also occupy the FR0 region in the luminosity-size plane. The strong overlap highlights that compact, confined radio sources are common manifestation of low-radio power AGN activity across both radio-selected and optically-selected samples. These comparisons underscore that the QFeedS sample maps onto the broader landscape of compact radio-AGN populations. While Pierce et al. highlights the role of host morphology, Chilufya et al. emphasizes the compactness and FR0-like character, with the QFeedS connecting these with the quasar regime of high radiative accretion, demonstrating how luminous quasars can host radio emission that mimics low-power radio galaxies. Overall, the QFeedS sample traces a continuum, from luminous quasars with extended jet-like structures, to compact, low-power systems whose radio emission resembles FR0s, thereby mapping the diversity of radio AGN activity across nearly four orders of magnitude in radio luminosity.

## 6 CONCLUSION

We present a new sample of  $29 z < 0.2$  quasars (QFeedS-2) with  $L_{1.4\text{GHz}} < 10^{23.45} \text{ W Hz}^{-1}$ , as an extension to our Quasar Feedback Survey (QFeedS; see Fig. 1). In this work, we study the gigahertz radio emission using new 1.4 GHz (L-band) and 6 GHz (C-band) data from the VLA, which cover a spatial resolution of  $\sim 1\text{--}3 \text{ kpc}$ . Our main conclusions are:

- For the vast majority of sources ( $\sim 80$  per cent), our L-band VLA imaging recovers the FIRST 1.4 GHz flux, indicating that the high-resolution maps capture the bulk of the total gigahertz emission.
- The gigahertz radio emission is extended on  $\sim 0.1\text{--}20 \text{ kpc}$  scales.  $31^{+9.1}_{-7.8}$  per cent of the sample show extended radio structures indicative of AGN-driven outflows (i.e., jet or wind-driven; Fig. 3). This is compared to the  $55^{+7.5}_{-7.7}$  per cent AGN-like extended radio structures for the more radio luminous QFeedS-1 quasars, which are also more likely to exhibit the most extended,  $\gtrsim 10 \text{ kpc}$  scale emission (Fig. 4).
- Nine of the quasars display collimated morphologies indicative of AGN (e.g., bipolar features, hot spots, S-shaped jets), although typically smaller in scale than classical FR I/II galaxies (Fig. 3; Jarvis et al. 2021; Njeri et al. 2025). Others (20/29) remain compact

(Fig. 2) and may host sub-kpc jets, thus requiring higher resolution radio imaging to confirm (e.g., Njeri et al. 2025).

- The majority (90 per cent) of the sample show very steep spectral indices across 5–7 GHz with  $\alpha \lesssim -1$ , potentially indicating a strong contribution from interactions between the AGN and ISM. Only three QFeedS-2 sources show radio emission dominated by AGN-core like emission, based on flat spectral indices or high brightness temperatures (see Fig. 5).

- Combining spectral indices, brightness temperatures, and morphology criteria, 11/29 of the targets (i.e.,  $38^{+9.3}_{-8.5}$  per cent) are confirmed as radio-AGN. This is compared to 28/42 ( $67^{+6.8}_{-7.6}$  per cent) following the same criteria, in the more radio luminous QFeedS-1 sample (Section 5.1; Fig. 6). However, the total fraction of QFeedS-1 confirmed as radio-AGN is 86 per cent based on additional data from *e*-MERLIN and far-infrared measurements; which are not currently available for QFeedS-2 (Fig. 6; Njeri et al. 2025). Hence, 38 per cent is considered a lower limit of radio-AGN in QFeedS-2. Overall,  $66^{+5.8}_{-5.9}$  per cent of the full QFeedS sample can be attributed to a radio-AGN origin.

- For the sources that are not identified as a radio-AGN ( $\sim 62^{+8.5}_{-9.3}$  per cent) in QFeedS-2, it is not possible to rule out a strong contribution of star formation to the radio emission. However, across the sample as a whole, the radio emission is unlikely to be star-formation dominated, due to the compact emission and very high inferred star formation rates at the radio luminosity range of the sample (Fig. 7).

- Across the whole of QFeedS, the Type 2 sources display a slightly higher incidence of extended radio structures (52 per cent compared to 32 per cent). Furthermore, at the highest radio luminosities, the Type 1 sources are more likely to be core-dominated (with high brightness temperatures and flat spectral indices), compared to the Type 2 sources (Fig. 6). These observations are broadly consistent with an orientation based model of AGN types.

- With  $\sim 80$  per cent of our QFeedS-2 sample falling in the FR0 region (Fig. 4), their radio properties would, at face value, be consistent with the classical FR0 population (Baldi et al. 2015; Baldi 2023). However, by construction, our sample is selected to have very high [O III] luminosities ( $L_{[\text{O III}]} \gtrsim 10^{42} \text{ erg s}^{-1}$ ), unambiguously pointing to radiatively efficient, high-accretion quasars. This highlights that FR0-like radio morphologies do not necessarily imply radiatively inefficient accretion (Section 5.3).

The Quasar Feedback Survey demonstrates that quasars, even those traditionally labeled radio quiet, are not radio silent but span a continuous spectrum of radio activity and feedback modes; from powerful jets in luminous systems to weaker, radio emission in lower-luminosity systems, likely associated with weak radio jets or outflows from quasar winds. These results emphasize that robust identification of radio-AGN in the radio-quiet regime requires high-resolution, multi-band radio data, ideally combined with multi-wavelength constraints.

Our QFeedS-1 sample, which represents the higher radio luminosities ( $L_{1.4\text{GHz}} \sim 10^{23.45\text{--}26.30} \text{ W Hz}^{-1}$ ), has already revealed that compact, AGN-driven jets and/or winds strongly couple to the ISM, driving significant multi-phase outflows (e.g. Jarvis et al. 2021; Girdhar et al. 2022; Silpa et al. 2022; Girdhar et al. 2024). However, these objects align with the classical ‘radio-intermediate’ population where compact but powerful radio activity is becoming a clear signature of feedback activity (Harrison & Ramos Almeida 2024). Follow-up observations of QFeedS-2 will assess the driving mechanisms and impact on the ISM of lower radio power systems. Thus, the combined QFeedS quasars, covering four orders of magnitude in radio luminos-

ity, represent a compelling laboratory for bridging radio-quiet and radio-loud AGN regimes, uncovering the diverse physical channels through which quasars generate radio emission, and how they can influence their galactic environments.

More broadly, current and future radio facilities (e.g., LOFAR-ILT, SKA and ngVLA; [Dewdney et al. 2009](#); [Murphy et al. 2018](#); [Morabito et al. 2025a](#)) will be transformative in understanding radio emission and related feedback processes across the whole AGN population. High-frequency arrays will unveil low power milliarcsecond jets unidentified in current radio maps, while low-frequency, high-sensitivity observations will capture aged, diffuse plasma, which is key to understanding the full lifecycle of AGN outflows. Integrating such radio diagnostics with X-ray observations, sub-mm interferometry and integral-field spectroscopy, will allow us to directly observe how compact jets or quasar-driven winds impact the surrounding ISM and assess their role in feedback processes in large, and representative, AGN samples.

## ACKNOWLEDGEMENTS

We thank the referee for their prompt and constructive report. AN, CMH, and VF acknowledge funding from an United Kingdom Research and Innovation grant (code: MR/V022830/1). PK acknowledges the support of the Department of Atomic Energy, Government of India, under the project 12-R&D-TFR-5.02-0700. DMA thanks the Science Technology Facilities Council (STFC) for support through the Durham consolidated grant (ST/T000244/1). SS acknowledges funding from ANID through Fondecyt Postdoctorado (project code 3250762), Millenium Nucleus NCN23\_002 (TITANs), and Comité Mixto ESO-Chile. We acknowledge the use of the ilifu cloud computing facility - [www.ilifu.ac.za](#), a partnership between the University of Cape Town, the University of the Western Cape, the University of Stellenbosch, Sol Plaatje University, the Cape Peninsula University of Technology and the South African Radio Astronomy Observatory.

## DATA AVAILABILITY

The data underlying this article were accessed from the NRAO Science Data Archive (<https://data.nrao.edu/portal/>) using the proposal id: 23A-214. The spectral index, C-band and L-band maps produced in this work, including the figures for all 29 targets showing the radio contours overlaid on the optical images (in the style of Figure 2) are all available at <https://doi.org/10.25405/data.ncl.c.8110946>. All public data related to the Quasar Feedback Survey can also be located via our website: <https://blogs.ncl.ac.uk/quasarfeedbacksurvey/data/>.

## REFERENCES

Abazajian K. N., et al., 2009, *ApJS*, **182**, 543  
 Ahumada R., et al., 2020, *ApJS*, **249**, 3  
 An T., Baan W. A., 2012, *ApJ*, **760**, 77  
 Audibert A., et al., 2023, *A&A*, **671**, L12  
 Baldi R. D., 2023, *A&ARv*, **31**, 3  
 Baldi R. D., Capetti A., Giovannini G., 2015, *A&A*, **576**, A38  
 Baldi R. D., et al., 2018, *MNRAS*, **476**, 3478  
 Baldi R. D., Giovannini G., Capetti A., 2021, *Galaxies*, **9**, 106  
 Becker R. H., White R. L., Helfand D. J., 1995, *ApJ*, **450**, 559  
 Begelman M. C., Blandford R. D., Rees M. J., 1984, *Reviews of Modern Physics*, **56**, 255  
 Behar E., Baldi R. D., Laor A., Horesh A., Stevens J., Tzioumis T., 2015, *MNRAS*, **451**, 517  
 Bernhard E., Tadhunter C. N., Pierce J. C. S., Dicken D., Mullaney J. R., Morganti R., Ramos Almeida C., Daddi E., 2022, *MNRAS*, **512**, 86  
 Bessiere P. S., Ramos Almeida C., Holden L. R., Tadhunter C. N., Canalizo G., 2024, *A&A*, **689**, A271  
 CASA Team 2022, IMFIT – Image analysis task (image fitting). National Radio Astronomy Observatory (NRAO) / CASA Development Team, <https://casa.nrao.edu/casadocs>  
 Calistro Rivera G., et al., 2024, *A&A*, **691**, A191  
 Chilufya J., Hardcastle M. J., Pierce J. C. S., Croston J. H., Mingo B., Zheng X., Baldi R. D., Röttgering H. J. A., 2024, *MNRAS*, **529**, 1472  
 Circosta C., et al., 2018, *A&A*, **620**, A82  
 Condon J. J., 1992, *ARA&A*, **30**, 575  
 Condon J. J., Condon M. A., Gisler G., Puschell J. J., 1982, *ApJ*, **252**, 102  
 Condon J. J., Huang Z.-P., Yin Q. F., Thuan T. X., 1991, *ApJ*, **378**, 65  
 Condon J. J., Cotton W. D., Greisen E. W., Yin Q. F., Perley R. A., Taylor G. B., Broderick J. J., 1998, *AJ*, **115**, 1693  
 Cresci G., et al., 2023, *A&A*, **672**, A128  
 Davies R., et al., 2020, *MNRAS*, **498**, 4150  
 Del Moro A., et al., 2013, *A&A*, **549**, A59  
 Delhaize J., et al., 2017, *A&A*, **602**, A4  
 Delvecchio I., et al., 2017, *A&A*, **602**, A3  
 Dewdney P. E., Hall P. J., Schilizzi R. T., Lazio T. J. L. W., 2009, *IEEE Proceedings*, **97**, 1482  
 Dey A., et al., 2019, *AJ*, **157**, 168  
 Eberhard J.-M., Reines A. E., Gim H. B., Darling J., Greene J. E., 2025, *ApJ*, **978**, 158  
 Fabian A. C., 2012, *ARA&A*, **50**, 455  
 Fawcett V. A., Alexander D. M., Rosario D. J., Klindt L., Fotopoulou S., Lusso E., Morabito L. K., Calistro Rivera G., 2020, *MNRAS*, **494**, 4802  
 Fawcett V. A., et al., 2025, *MNRAS*, **537**, 2003  
 Fluetsch A., et al., 2021, *MNRAS*, **505**, 5753  
 García-Burillo S., et al., 2021, *A&A*, **652**, A98  
 Girdhar A., et al., 2022, *MNRAS*, **512**, 1608  
 Girdhar A., et al., 2024, *MNRAS*, **527**, 9322  
 Godfrey L. E. H., Shabala S. S., 2016, *MNRAS*, **456**, 1172  
 Hardcastle M. J., Croston J. H., 2020, *New Astron. Rev.*, **88**, 101539  
 Hardcastle M. J., et al., 2025, *MNRAS*, **539**, 1856  
 Harrison C. M., 2017, *Nature Astronomy*, **1**, 0165  
 Harrison C. M., Ramos Almeida C., 2024, *Galaxies*, **12**, 17  
 Harrison C. M., Alexander D. M., Mullaney J. R., Swinbank A. M., 2014, *MNRAS*, **441**, 3306  
 Harrison C. M., Thomson A. P., Alexander D. M., Bauer F. E., Edge A. C., Hogan M. T., Mullaney J. R., Swinbank A. M., 2015, *ApJ*, **800**, 45  
 Harwood J. J., et al., 2022, *A&A*, **658**, A8  
 Heckman T. M., Best P. N., 2014, *Annual Review of Astronomy and Astrophysics*, **52**, 589  
 Helou G., Soifer B. T., Rowan-Robinson M., 1985, *ApJ*, **298**, L7  
 Ilha G. S., et al., 2025, *arXiv e-prints*, p. arXiv:2510.14152  
 Ivezić Ž., et al., 2002, *AJ*, **124**, 2364  
 Jackson T. M., Rosario D. J., Alexander D. M., Scholtz J., McAlpine S., Bower R. G., 2020, *MNRAS*, **498**, 2323  
 Jarvis M. E., et al., 2019, *MNRAS*, **485**, 2710  
 Jarvis M. E., et al., 2020, *MNRAS*, **498**, 1560  
 Jarvis M. E., et al., 2021, *MNRAS*, **503**, 1780  
 Karouzos M., Woo J.-H., Bae H.-J., 2016, *ApJ*, **819**, 148  
 Kellermann K. I., Sramek R., Schmidt M., Shaffer D. B., Green R., 1989, *AJ*, **98**, 1195  
 Kellermann K. I., Condon J. J., Kimball A. E., Perley R. A., Ivezić Ž., 2016, *ApJ*, **831**, 168  
 Kennicutt R. C., Evans N. J., 2012, *ARA&A*, **50**, 531  
 Kewley L. J., Heisler C. A., Dopita M. A., Sutherland R., Norris R. P., Reynolds J., Lumsden S., 2000, *ApJ*, **530**, 704  
 Kharb P., Silpa S., 2023, *Galaxies*, **11**, 27  
 Kharb P., Vaddi S., Sebastian B., Subramanian S., Das M., Paragi Z., 2019, *ApJ*, **871**, 249  
 Kharb P., Subramanian S., Das M., Vaddi S., Paragi Z., 2021, *ApJ*, **919**, 108

Klindt L., Alexander D. M., Rosario D. J., Lusso E., Fotopoulou S., 2019, *MNRAS*, **488**, 3109

Kunert-Bajraszewska M., Gawroński M. P., Labiano A., Siemiginowska A., 2010, *MNRAS*, **408**, 2261

Laing R. A., Peacock J. A., 1980, *MNRAS*, **190**, 903

Lansbury G. B., Jarvis M. E., Harrison C. M., Alexander D. M., Del Moro A., Edge A. C., Mullaney J. R., Thomson A. P., 2018, *ApJ*, **856**, L1

Laor A., Behar E., 2008, *MNRAS*, **390**, 847

Liao M., Wang J., Ren W., Zhou M., 2024, *MNRAS*, **528**, 3696

Magliocchetti M., Popesso P., Brusa M., Salvato M., 2018, *MNRAS*, **473**, 2493

Marvil J., Owen F., Eilek J., 2015, *AJ*, **149**, 32

McCaffrey T. V., Kimball A. E., Momjian E., Richards G. T., 2022, *AJ*, **164**, 122

McMullin J. P., Waters B., Schiebel D., Young W., Golap K., 2007, Astronomical Data Analysis Software and Systems XVI ASP Conference Series, 376, 127

Meenakshi M., et al., 2022, *MNRAS*, **516**, 766

Meenakshi M., Mukherjee D., Bodo G., Rossi P., Harrison C. M., 2024, *MNRAS*, **533**, 2213

Middleberg E., Agudo I., Roy A. L., Krichbaum T. P., 2007, *MNRAS*, **377**, 731

Mingo B., et al., 2022, *MNRAS*, **511**, 3250

Molyneux S. J., et al., 2024, *MNRAS*, **527**, 4420

Mooley K. P., et al., 2016, *ApJ*, **818**, 105

Morabito L. K., et al., 2022, *MNRAS*, **515**, 5758

Morabito L. K., et al., 2025a, *Ap&SS*, **370**, 19

Morabito L. K., et al., 2025b, *MNRAS*, **536**, L32

Morganti R., Tadhunter C. N., Oosterloo T. A., 2005, *A&A*, **444**, L9

Morganti R., Murthy S., Guillard P., Oosterloo T., Garcia-Burillo S., 2023, *Galaxies*, **11**, 24

Mukherjee D., 2025, *arXiv e-prints*, p. arXiv:2506.03888

Mukherjee D., Bicknell G. V., Wagner A. Y., Sutherland R. S., Silk J., 2018, *MNRAS*, **479**, 5544

Mullaney J. R., Alexander D. M., Fine S., Goulding A. D., Harrison C. M., Hickox R. C., 2013, *MNRAS*, **433**, 622

Murphy E. J., et al., 2011, *ApJ*, **737**, 67

Murphy E. J., et al., 2018, in Murphy E., ed., Astronomical Society of the Pacific Conference Series Vol. 517, Science with a Next Generation Very Large Array. p. 3 (arXiv:1810.07524), doi:10.48550/arXiv.1810.07524

Nesvadba N. P. H., De Breuck C., Lehnert M. D., Best P. N., Collet C., 2017, *A&A*, **599**, A123

Nims J., Quataert E., Faucher-Giguère C.-A., 2015, *MNRAS*, **447**, 3612

Njeri A., et al., 2023, *MNRAS*, **519**, 1732

Njeri A., et al., 2025, *MNRAS*, **537**, 705

O'Dea C. P., 1998, *PASP*, **110**, 493

O'Dea C. P., Saikia D. J., 2021, *A&ARv*, **29**, 3

Ofek E. O., Frail D. A., 2011, *ApJ*, **737**, 45

Padovani P., 2016, *A&ARv*, **24**, 13

Padovani P., 2017, *Nature Astronomy*, **1**, 0194

Panessa F., Baldi R. D., Laor A., Padovani P., Behar E., McHardy I., 2019, *Nature Astronomy*, **3**, 387

Perley R. A., Butler B. J., 2013, *ApJS*, **204**, 19

Pierce J. C. S., Tadhunter C. N., Morganti R., 2020, *MNRAS*, **494**, 2053

Radcliffe J. F., et al., 2018, *A&A*, **619**, A48

Radcliffe J. F., Beswick R. J., Thomson A. P., Garrett M. A., Barthel P. D., Muxlow T. W. B., 2019, *MNRAS*, **490**, 4024

Ramos Almeida C., et al., 2022, *A&A*, **658**, A155

Rao V. V., et al., 2023, *MNRAS*, **524**, 1615

Riffel R. A., Storchi-Bergmann T., Riffel R., Dahmer-Hahn L. G., Diniz M. R., Schönell A. J., Dametto N. Z., 2017, *MNRAS*, **470**, 992

Rosario D. J., Fawcett V. A., Klindt L., Alexander D. M., Morabito L. K., Fotopoulou S., Lusso E., Calistro Rivera G., 2020, *MNRAS*, **494**, 3061

Rose M., Tadhunter C., Ramos Almeida C., Rodríguez Zaurín J., Santoro F., Spence R., 2018, *MNRAS*, **474**, 128

Roy N., Heckman T., Henry A., 2025, *arXiv e-prints*, p. arXiv:2508.06707

Sabater J., et al., 2019, *A&A*, **622**, A17

Santoro F., Tadhunter C., Baron D., Morganti R., Holt J., 2020, *A&A*, **644**, A54

Shimizu T. T., Mushotzky R. F., Meléndez M., Koss M. J., Barger A. J., Cowie L. L., 2017, *MNRAS*, **466**, 3161

Silpa S., Kharb P., Ho L. C., Ishwara-Chandra C. H., Jarvis M. E., Harrison C., 2020, *MNRAS*, **499**, 5826

Silpa S., Kharb P., Harrison C. M., Girdhar A., Mukherjee D., Mainieri V., Jarvis M. E., 2022, *MNRAS*, **513**, 4208

Silpa S., Kharb P., Ho L. C., Harrison C. M., 2023, *ApJ*, **958**, 47

Slob M. M., Callingham J. R., Röttgering H. J. A., Williams W. L., Duncan K. J., de Gasperin F., Hardcastle M. J., Miley G. K., 2022, *A&A*, **668**, A186

Smolčić V., et al., 2017, *A&A*, **602**, A6

Speranza G., et al., 2021, *A&A*, **653**, A150

Tadhunter C., 2016, *Astronomische Nachrichten*, **337**, 159

Tanner R., Weaver K. A., 2022, *AJ*, **163**, 134

Ulivi L., et al., 2024, *A&A*, **685**, A122

Ulvestad J. S., Antonucci R. R. J., Barvainis R., 2005, *ApJ*, **621**, 123

Venturi G., et al., 2021, *A&A*, **648**, A17

Villar Martín M., Emonts B. H. C., Cabrera Lavers A., Bellocchi E., Alonso Herrero A., Humphrey A., Dall'Agnol de Oliveira B., Storchi-Bergmann T., 2021, *A&A*, **650**, A84

Wang Y., et al., 2024, *A&A*, **685**, A79

White S. V., Jarvis M. J., Häußler B., Maddox N., 2015, *MNRAS*, **448**, 2665

White S. V., Jarvis M. J., Kalfountzou E., Hardcastle M. J., Verma A., Cao Orjales J. M., Stevens J., 2017, *MNRAS*, **468**, 217

Woo J.-H., Bae H.-J., Son D., Karouzos M., 2016, *ApJ*, **817**, 108

Xu C., Livio M., Baum S., 1999, *AJ*, **118**, 1169

Yun M. S., Reddy N. A., Condon J. J., 2001, *ApJ*, **554**, 803

Zakamska N. L., Greene J. E., 2014, *MNRAS*, **442**, 784

Zakamska N. L., Strauss M. A., Heckman T. M., Ivezić Ž., Krolik J. H., 2004, *AJ*, **128**, 1002

Zakamska N. L., et al., 2016, *MNRAS*, **455**, 4191

de Vries W. H., Becker R. H., White R. L., Helfand D. J., 2004, *AJ*, **127**, 2565

This paper has been typeset from a  $\text{\TeX}$ / $\text{\LaTeX}$  file prepared by the author.